

We thank the two anonymous reviewers for their valuable comments and constructive suggestions on the manuscript. Below, we explain how the comments and suggestions are addressed and make note of the revision in the revised manuscript.

Reviewer #1

In this paper, the authors evaluate cloud properties as simulated with the Community Atmosphere Model Version 5 (CAM5) against observations for the HIAPER Pole-to-Pole Observations (HIPPO). To conduct a direct comparison, the model was nudged to be more representative in respect to the reanalysis. The authors show that underestimation of water vapor is responsible for most of cloud occurrence biases. They also discuss the sensitivity of autoconversion of ice to snow and ice nucleation to the modeled cloud microphysical properties as compared against observations. This paper is well written and of scientific relevance. I have a few minor comments/suggestions I would like to be addressed before publication.

Reply: We thank the reviewer for constructive review and encouraging comments. The text and figures are revised as the reviewer suggested.

Introduction: Page 3, line 51. I would start the introduction with: “Cirrus clouds, located at high altitudes and composed of ice crystals, are one of the key components in the climate system. They cover about 30%.....”

Reply: Done.

Page 4, line 75: I suggest replace “higher” with “high” (since there are no mention yet what nucleates at lower supersaturations), and the give a typical range of supersaturations.

Reply: We changed the text “Homogeneous nucleation generally requires higher supersaturation” to “Homogeneous nucleation generally requires high ice supersaturation typically of 40%-60%” in the revised manuscript.

Page 4, line 83: Replace “ice microphysics” with “ice microphysical processes”

Reply: Done.

Page 5, line 110: What is meant by fast measurements? High frequency measurements?

Reply: Yes, we meant high frequency measurements. We changed “fast measurements” to “high frequency measurements” in the revised manuscript.

Page 67, line 140. What about observations of water vapor? Since much of the analysis is in regard to the relative humidity and supersaturation, I think the observations of water vapor should be included as well.

Reply: Thank the reviewer for this comment. We included “water vapor” in describing “measurements of ambient environmental conditions” in the revised manuscript.

Page 12, line 248: Replace “the” with “for”

Reply: Done.

Page 12, line 256, add “a” between “includes version”, so that “includes a version”

Reply: Done.

Page 16, line 340. “Reword CAM5 is able to better simulate cloud systems”

Reply: Done.

Page 21, line 465. I suggest to rewrite: “The model is capable to simulate the occurrences of ice” i.e. remove the reference to comparison with observations, since the model does a poor job in simulating supersaturation in clear sky.

Reply: Done.

Page 568, line 568 (or figure 8F). The point of DCS75 and PRE-ICE can produce $N_i > 50 \text{ L}^{-1}$ is hard to see because the figure is too small.

Reply: Thank you for pointing out this. We added an inset with rescaled axes in Figure 8f to illustrate the frequency of N_i when $N_i > 50 \text{ L}^{-1}$. From the inset, it is clear that DCS75 and PRE-ICE can produce $N_i > 50 \text{ L}^{-1}$.

Page 31, line 678: Replace “which nudge the” with “with nudged”. Page 32, line 688. Remove “and” before 86.1% Page 32, line 691: Remove “of” Page 32, line 705: Add “to” so that “The model is mostly able to reproduce...” Page 34, line 735. Suggest adding “global” such that “...future global model....”

Reply: All the suggested revisions are done in the revised manuscript.

Page 34, line 746. A recently published paper by Eidhammer et al. (2017) describes the implementation of the single ice category in CAM5. I suggest including this citation on line 746.

Eidhammer, T., H. Morrison, D. Mitchell, A. Gettelman, and E. Erfani, 2017: Improvements in Global Climate Model Microphysics Using a Consistent Representation of Ice Particle Properties. J. Climate, 30, 609–629, doi: 10.1175/JCLI-D-16-0050.1.

Reply: We thank the reviewer for pointing us to the work of Eidhammer et al. (2017), which is very relevant to our study. We have cited their study for references in the revised version.

We thank the two anonymous reviewers for their valuable comments and constructive suggestions on the manuscript. Below, we explain how the comments and suggestions are addressed and make note of the revision in the revised manuscript.

Reviewer #2

The Community Atmosphere Model Version 5 (CAM5) is evaluated using HIPPO measurements in this study. It shows that CAM5 can reproduce most of the observed cloud systems. This study also pointed out that the missing cloud occurrences in the model simulations are mostly attributed to the discrepancies in water vapor, and further improvements to RH variability are needed in the model.

The manuscript is overall well-written and delivers the necessary information concisely. Some revisions are needed to address the following questions before the acceptance of this manuscript:

Reply: We thank the reviewer for his/her helpful comments. The text and figures are revised as the reviewer suggested.

1. Lines 269-271: Please check grammar.

Reply: We changed the sentence to “**We also conduct two experiments, one with only U and V nudged (referred to as NUG_UV) and the other with U, V, T and water vapor (Q) nudged (referred to as NUG_UVTQ)**” in the revised manuscript.

2. Lines 271-272: This study uses horizontal resolution of 1.9 degree x 2.5 degree. CAM5 can be run at much higher resolution, such as 0.23 degree x 0.31 degree, which may be more appropriate for comparison with HIPPO aircraft observations and help address the over-sample issue that the authors also mentioned (lines 293-311). Please justify why a higher resolution is not used in this study.

Reply: Although CAM5 can be run at higher resolutions, we choose the resolution of 1.9 degree x 2.5 degree in this study because this resolution is still widely used in CAM5 simulations and in other climate model simulations. We prefer to first evaluate the model performance at this resolution before we move to higher resolutions. As mentioned in Section 6 (Discussion and Conclusions), understanding the resolution dependence of model results is also desirable and we plan to investigate it in the near future. In particular, as the reviewer pointed out, using higher resolutions will help address the

over-sample issue in the comparison with observations in the present study, which will also be examined. We have added the above justifications in the revised manuscript.

3. Figure 1: Different colors for HIPPO observations (especially for ice clouds and warm clouds) should be used to distinguish the modeled results and observations.

Reply: Following the reviewer's suggestion, different colors for HIPPO observations (i.e., violet and brown for ice clouds and warm clouds, respectively) are used to distinguish the modeled results and observations in the revised manuscript.

4. Lines 525-526: Why there are more large ice particles at higher temperature? Is it because that it is more likely for heterogeneous nucleation (formation of larger ice crystals) to occur at higher temperature than homogeneous nucleation (formation of smaller ice crystals)?

Reply: We thank the reviewer for the comment. The relationship between slope parameter and temperature depends not only on ice nucleation but also on ice crystal growth. With increasing temperature (or decreasing height), there is more water vapor available for the growth of ice crystals (due to increased saturation vapor pressure), which can partly explain the decreasing trend of slope parameter with temperature. In addition, as mentioned by the reviewer, it is more likely for heterogeneous ice nucleation to occur at higher temperature than homogeneous nucleation and the former process tends to form less ice crystals to produce larger ice crystals (due to less competition for the available water vapor). In the revised manuscript, we revised the explanation to make it clearer: “Such a feature is mainly due to more small ice particles at lower temperatures, which can be explained by less water vapor available for ice crystal growth as well as more ice crystals formed from nucleation at lower temperatures (more likely from homogeneous nucleation than from heterogeneous nucleation) (Eidhammer et al., 2014).”

5. Line 581-586: When all sulfate aerosol particles are available for homogeneous nucleation, it seems to me that more ice crystals with smaller size should be formed, and N_i (number of particles larger than 75 μm) should decrease.

Reply: We thank the reviewer for pointing out the consistency between ice crystal size (in term of slope parameter) and N_i (number concentration of ice crystals larger than 75 μm). When all sulfate aerosol particles are available for homogeneous nucleation, the slope parameter for the gamma size distribution is much larger in SUL, indicating a larger

fraction of ice crystals with smaller size and a smaller fraction of ice crystals with larger size (Figure 7). However, as total ice crystal number concentration in SUL is much higher (one to two orders magnitude larger) than that in CTL, especially at lower temperature, overall N_i in SUL does not decrease but increases compared to that in CTL (Figure 9). In the revised version, we added the explanation for the difference of N_i between SUL and CTL: “With the removal of the lower size limit (0.1 μm diameter) of sulfate aerosol particles for homogeneous nucleation in the experiment SUL, simulated N_i is significantly higher than that in CTL because of the substantial increase in the total ice crystal number concentration in SUL, although the slope parameter in SUL is larger indicating a smaller fraction of ice crystals with larger sizes (e.g., larger than 75 μm).”

6. Lines 649-652: In previous section (Section 4.1), it is shown that the missing cloud occurrences in the model simulations are primarily ascribed to the fact that the model cannot account for the high spatial variability of observed relative humidity (RH), and that model RH biases are mostly attributed to the discrepancies in water vapor. Here it shows that when nudging both T and Q together with U and V, the model performance is even worse in terms of cloud simulations. Since the model produces clouds based on RH values, is it possible that the worse simulation of clouds in the NUG_UVTQ experiment is related to the RH threshold values used in the model?

Reply: We thank the review for this constructive comment. Indeed, the model simulation of cloud occurrences is sensitive to RH threshold used in the calculation of cloud fraction. For instance, with a smaller RH threshold (RH_{min}), the model can simulate larger cloud fraction and produce cloud occurrences at lower grid-mean RH. In NUG_UVTQ, although Q is nudged in the model, the model simulates worse cloud occurrences. It is possible that discrepancy in the cloud fraction scheme (e.g., the chosen RH_{min}) may also partly contribute to the degradation of simulation. Following the reviewer’s comment, we added the discussion in Section 5 in the revised manuscript: “The bias in cloud occurrences may also be related to the RH threshold values used in the cloud fraction scheme in the model (Park et al., 2014), and further study is needed to address the model sensitivity to the RH threshold values.”

1 **Direct comparisons of ice cloud macro- and microphysical properties**
2 **simulated by the Community Atmosphere Model version 5 with**
3 **HIPPO aircraft observations**

4 Chenglai Wu^{1,2}, Xiaohong Liu^{1,*}, Minghui Diao³, Kai Zhang⁴, Andrew Gettelman⁵,
5 Zheng Lu¹, Joyce E. Penner⁶, and Zhaohui Lin²

6 ¹*Department of Atmospheric Science, University of Wyoming, Laramie, Wyoming,*
7 *USA*

8 ²*International Center for Climate and Environment Sciences, Institute of Atmospheric*
9 *Physics, Chinese Academy of Sciences, Beijing, China*

10 ³*Department of Meteorology and Climate Science, San Jose State University, San*
11 *Jose, California, USA*

12 ⁴*Pacifit Northwest National Laboratory, Richland, Washington, USA*

13 ⁵*National Center for Atmospheric Research, Boulder, Colorado, USA*

14 ⁶*Department of Climate and Space Sciences and Engineering, University of Michigan,*
15 *Ann Arbor, Michigan, USA*

16
17 **Corresponding to:*

18
19 Xiaohong Liu
20 Department of Atmospheric Science
21 University of Wyoming
22 Dept. 3038, 1000 East University Avenue
23 Laramie, WY 82071
24 Email: xliu6@uwyo.edu.

25
26
27

28 **Abstract**

29 In this study we evaluate cloud properties simulated by the Community
30 Atmosphere Model Version 5 (CAM5) using in-situ measurements from the HIAPER
31 Pole-to-Pole Observations (HIPPO) for the period of 2009 to 2011. The modeled
32 wind and temperature are nudged towards reanalysis. Model results collocated with
33 HIPPO flight tracks are directly compared with the observations, and model
34 sensitivities to the representations of ice nucleation and growth are also examined.
35 Generally, CAM5 is able to capture specific cloud systems in terms of vertical
36 configuration and horizontal extension. In total, the model reproduces 79.8% of
37 observed cloud occurrences inside model grid boxes, and even higher (94.3%) for ice
38 clouds ($T \leq -40^\circ\text{C}$). The missing cloud occurrences in the model are primarily ascribed
39 to the fact that the model cannot account for the high spatial variability of observed
40 relative humidity (RH). Furthermore, model RH biases are mostly attributed to the
41 discrepancies in water vapor, rather than temperature. At the micro-scale of ice clouds,
42 the model captures the observed increase of ice crystal mean sizes with temperature,
43 albeit with smaller sizes than the observations. The model underestimates the
44 observed ice number concentration (N_i) and ice water content (IWC) for ice crystals
45 larger than $75 \mu\text{m}$ in diameter. Modeled IWC and N_i are more sensitive to the
46 threshold diameter for autoconversion of cloud ice to snow (D_{cs}), while simulated ice
47 crystal mean size is more sensitive to ice nucleation parameterizations than to D_{cs} .
48 Our results highlight the need for further improvements to the sub-grid RH variability
49 and ice nucleation and growth in the model.

50 **1 Introduction**

51 Cirrus clouds, located at high altitudes and composed of ice crystals, are one of
52 the key components in the climate system. They cover about 30% of the globe (Wang
53 et al., 1996; Wylie and Menzel, 1999). They have a significant impact on the earth's
54 radiation balance via two different effects: scattering and reflecting the incoming
55 short wave solar radiation back to space, which leads to a cooling effect on the planet;
56 and absorbing and re-emitting terrestrial longwave radiation, leading to a warming
57 effect (Liou, 1986; Ramanathan and Collins, 1991; Corti et al., 2005). The net
58 radiative effect is thus a balance of these two effects and mainly depends on the
59 amount, microphysical and optical properties of cirrus clouds (Kay et al., 2006;
60 Fusina et al., 2007; Gettelman et al., 2012; Tan et al., 2016). Furthermore, as the
61 efficiency of dehydration at the tropical tropopause layer is strongly influenced by the
62 microphysical processes within cirrus clouds, cirrus clouds can also regulate the
63 humidity of air entering the stratosphere and are recognized as an important
64 modulator for water vapor in the upper troposphere and the lower stratosphere
65 (Gettelman et al., 2002; Wang and Penner, 2010; Jensen et al., 2013; Dinh et al.,
66 2014).

67 Despite their important role in the climate system, there are still large
68 uncertainties in the representation of cirrus clouds in global climate models (GCMs)
69 (Boucher et al., 2013). The uncertainties are the result of several different aspects.
70 First, our understanding of processes initiating the cirrus cloud formation is still
71 limited (DeMott et al., 2003; Kärcher and Spichtinger, 2009; Hoose and Möhler,

User 2/23/2017 4:01 PM

Deleted: the type of clouds

User 2/23/2017 4:01 PM

Deleted: Cirrus clouds

74 2012). Ice crystals can form via the homogeneous nucleation of soluble aerosol
75 particles and the heterogeneous nucleation associated with insoluble or partly
76 insoluble aerosol particles (e.g., Hagg et al., 2003; Liu and Penner, 2005; Wang and
77 Liu, 2014). Homogeneous nucleation generally requires high ice supersaturation
78 typically of 40%-60% and occurs at temperatures colder than about -37°C. It can be
79 fairly well represented by nucleation theory based on laboratory results (Koop et al.,
80 2000). Heterogeneous nucleation is initiated by certain types of aerosols (e.g., mineral
81 dust and biological aerosols) that act as ice nucleating particles (INP), which can
82 nucleate ice particles at significantly lower ice supersaturations in the environment.
83 Currently there are still large unknowns about the types of aerosol, modes of action
84 (e.g., immersion/condensation, deposition, contact), and the efficiencies of
85 heterogeneous nucleation in the atmosphere (Hoose and Möhler, 2012). Other ice
86 microphysical processes (e.g., ice aggregation, deposition/sublimation, and
87 sedimentation), as well as interactions among cirrus microphysical properties,
88 macroscopic properties (e.g., spatial extent), and meteorological fields could further
89 render the interpretation of observed ice cloud properties challenging (Diao et al.,
90 2013; Krämer et al., 2016).

91 In addition to our limited understanding of ice microphysical processes, it is
92 difficult for GCMs with coarse spatial resolution (e.g., tens to hundreds of kilometers
93 in the horizontal direction, and a kilometer in the vertical) to capture the sub-grid
94 variability of dynamical and microphysical processes that are vital for ice cloud
95 formation and evolution. The observed microphysical properties of cirrus clouds vary

User 2/23/2017 4:02 PM

Deleted: er

Xiaohong Liu 3/9/2017 1:41 PM

Deleted: (e.g., in excess

User 2/23/2017 4:26 PM

Deleted: s

99 significantly in time and space (e.g., Hoyle et al., 2005; Diao et al., 2013; Jensen et al.,
100 2013; Diao et al., 2014a), associated with variability in relative humidity, temperature,
101 and vertical wind speed. The spatial extent of clouds is represented in GCMs by
102 diagnosing the cloud fraction in individual model grid boxes using a parameterization.
103 Such a cloud fraction representation needs to be validated with observations in order
104 to identify model biases and to elucidate the reasons behind these biases for future
105 model improvement.

106 Two types of observational data are currently available for validating modeled
107 cirrus cloud properties: in-situ aircraft measurements (e.g., Krämer et al., 2009;
108 Lawson et al., 2011; Diao et al., 2013), and remote-sensing data from space-borne or
109 ground-based instruments (Mace et al., 2005; Deng et al., 2006, 2008; Li et al., 2012).
110 Remote-sensing data may not be directly comparable to model simulations due to the
111 sampling and algorithmic differences between GCM results and remote-sensing
112 retrievals unless a proper simulator, i.e. a so called “satellite simulator”, is adopted
113 (Bodas-Salcedo et al., 2011; Kay et al., 2012). In-situ aircraft observations can
114 provide direct measurements of ice crystal properties such as ice crystal number
115 concentration and size distribution. In particular, these observations are a good source
116 of accurate and high frequency measurements, and thus provide a unique tool for
117 constraining GCM cirrus parameterizations (e.g., Zhang et al., 2013; Eidhammer et al.,
118 2014). However, the grid scales of GCMs are much larger than those sampled by
119 in-situ observations. Thus direct comparisons at model grid scales are often hindered
120 unless in-situ observations are adequately distributed within the grid boxes and can be

User 2/23/2017 4:49 PM

Deleted: fast

122 scaled up. At the micro-scale level of cirrus clouds (sub-grid scale), statistical
123 comparisons between model simulations and in-situ observations, especially in terms
124 of relationships among cloud microphysical and meteorological variables, are
125 desirable to provide a reliable evaluation of model microphysics (e.g., Zhang et al.,
126 2013; Eidhammer et al., 2014). In addition, aircraft measurements are often limited in
127 their spatial and temporal coverage, which in some sense limits the scope of
128 model-observation comparisons that can be conducted.

129 Previous studies have focused on the evaluation of cirrus clouds from
130 free-running GCM simulations against in-situ observations (e.g., Wang and Penner,
131 2010; Zhang et al., 2013; Eidhammer et al., 2014). However, since the model
132 meteorology was not constrained by conditions that were representative of the time of
133 the observations, the model biases could not be exclusively ascribed to errors in the
134 cirrus parameterizations. Recently, a nudging technique has been developed to allow
135 the simulated meteorology to be more representative of global reanalysis/analysis
136 fields, and thus the comparison between model simulations and observations is more
137 straightforward for the interpretation and attribution of model biases (Kooperman et
138 al., 2012; Zhang et al., 2014). In such simulations, as the meteorology (winds and
139 temperatures) in the GCM are synchronized with observed meteorology, direct
140 comparisons can be achieved by selecting model results that are collocated with
141 observations in space and time, and thus the model outputs can be evaluated in a more
142 rigorous manner.

143 In this study, we use the in-situ aircraft measurements from the NSF HIAPER

144 Pole-to-Pole Observations (HIPPO) campaign (Wofsy et al., 2011) to evaluate the
145 cloud properties simulated by the Community Atmosphere Model version 5 (CAM5).
146 During the HIPPO campaign, high-resolution (~230 m, 1Hz) and comprehensive
147 measurements of ambient environmental conditions (such as air temperature, pressure,
148 [water vapor](#), and wind speed), cloud ice crystals and droplets were obtained. HIPPO
149 also provides a nearly pole-to-pole spatial coverage and relatively long flight hours
150 (~400 hours in total) in various seasons, making it a valuable dataset for GCM
151 evaluations. To facilitate the evaluation, CAM5 is run with specified dynamics where
152 the model meteorological fields (horizontal winds (U, V) and temperature (T)) are
153 nudged towards the NASA GEOS-5 analysis, while water vapor, cloud hydrometeors
154 and aerosols are calculated interactively by the model (Lamarque et al., 2012).
155 Moreover, we select collocated CAM5 output along the HIPPO aircraft flight tracks,
156 and compare the model simulations and observations directly. Our comparisons focus
157 on cloud occurrence, and cloud microphysical properties (e.g., ice water content,
158 number concentration and size distribution of ice particles) with a specific focus on
159 cirrus clouds. We also investigate the sensitivities of model simulated cirrus cloud
160 properties to the ice microphysics parameterizations as well as to the large scale
161 forcing associated with the nudging strategy.

162 The remainder of the paper is organized as follows. In section 2, we introduce the
163 HIPPO observational dataset and instrumentations. The model simulations and
164 experimental design are described in section 3. In section 4, we examine the model
165 performance in simulating cirrus cloud occurrence and microphysical properties and

Xiaohong Liu 3/9/2017 2:16 PM

Deleted:

167 investigate the reasons behind the model biases. Sensitivities of model results to
168 different nudging strategies are presented in section 5, and discussions and
169 conclusions in section 6.

170

171 **2 HIPPO aircraft observations**

172 The NSF HIPPO Global campaign provided comprehensive observations of
173 clouds and aerosols from 87°N to 67°S over the Pacific region during 2009 to 2011
174 (Wofsy et al., 2011). Observations were acquired using the National Science
175 Foundation's Gulfstream V (GV) research aircraft operated by the National Center for
176 Atmospheric Research (NCAR). During this three-year period, five HIPPO
177 deployments were carried out, with each deployment lasting from 23 days to about
178 one month. In total, the HIPPO campaign included 64 flights, 787 vertical profiles
179 (from the surface to up to 14 km), and 434 hours of high-rate measurements
180 (<http://hippo.ucar.edu>). In this study, we use the 1-Hz in-situ measurements of water
181 vapor, temperature, number concentration and size distribution of ice crystals as well
182 as the number concentration of cloud liquid droplets from HIPPO#2-5. HIPPO#1 did
183 not have ice probes onboard.

184 Water vapor was measured by the 25 Hz, open-path Vertical Cavity Surface
185 Emitting Laser (VCSEL) hygrometer (Zondlo et al., 2010). The accuracy and
186 precision of water vapor measurements was ~6% and $\leq 1\%$, respectively.
187 Temperature (T) was recorded by the Rosemount temperature probe. The accuracy
188 and precision of T measurements was 0.5 K and 0.01 K, respectively. Here saturation

189 vapor pressure is calculated following Murphy and Koop (2005), who stated that all
190 the commonly used expressions for the saturation vapor pressure over ice are within 1%
191 in the range between 170 and 273 K. Then we calculate relative humidity (RH) using
192 the saturation vapor pressure with respect to water ($T > 0^\circ\text{C}$) or with respect to ice
193 ($T \leq 0^\circ\text{C}$). Unless explicitly stated otherwise, we refer to RH with respect to water
194 when $T > 0^\circ\text{C}$ and RH with respect to ice when $T \leq 0^\circ\text{C}$.

195 Ice crystal concentrations were measured by the two-dimensional cloud particle
196 imaging (2DC) ice probe (Korolev et al., 2011). The 2DC measures ice crystals with a
197 64-diode laser array at 25 μm resolution and the corresponding size range of 25 –
198 1600 μm . Outside this range, ice crystals between 1600 μm and 3200 μm are
199 mathematically reconstructed. A quality control was further applied to filter out the
200 particles with sizes below 75 μm in order to minimize the shattering effect and optical
201 uncertainties associated with 2DC data. Thus the number concentration (N_i) of ice
202 crystals with diameter from 75 μm to 3200 μm (binned by 25 μm) was derived and is
203 used here for model comparisons. The ice water content (IWC) is derived by
204 integrating the ice crystal mass at each size bin. Mass is calculated from diameter and
205 N_i using the mass-dimension (m - D) relationship of Brown and Francis (1995). For the
206 ice crystal size distribution, a gamma function is assumed as in CAM5 (Morrison and
207 Gettelman, 2008):

$$208 \quad \phi(D) = N_0 D^\mu \exp(-\lambda D) \quad (1)$$

209 where D is diameter, N_0 is the intercept parameter, μ is the shape parameter which is
210 set to 0 currently, and λ is the slope parameter. The slope and intercept for the

211 observed ice crystal size distributions are obtained by fitting Eq. (1) using the least
212 squares method as described in Heymsfield et al. (2008). Observed size distributions
213 that provided less than five bins of non-zero concentrations are not considered in
214 order to maintain a reasonable fit, which is similar to what was done in Eidhammer et
215 al. (2014). This removes about 8% of the total 1-Hz observations of ice clouds
216 ($T \leq -40^\circ\text{C}$). Furthermore, we only retain those fitted size distributions that are well
217 correlated with the measured ones, i.e., with a correlation coefficient larger than 0.6,
218 which leads to a further removal of 10% of the total 1-Hz ice crystal measurements.
219 Note that these screenings are applied only for the derivation of the slope and
220 intercept parameters for the ice crystal size distribution.

221 The cloud droplet number concentration (N_d) was measured by the Cloud Droplet
222 Probe (CDP) during the HIPPO campaign. The CDP measurement range of cloud
223 droplet diameter is 2-50 μm . Because 2DC and CDP probes may report both ice
224 crystals and liquid droplets, we adopted a rigorous criteria for the detection of clouds
225 in different temperature ranges. 99% of the observed N_i are greater than 0.1 L^{-1} , thus a
226 threshold of 0.1 L^{-1} is used to define in-cloud conditions. For $T \leq -40^\circ\text{C}$, we use the
227 criterion of $N_i > 0.1 \text{ L}^{-1}$ to detect the occurrence of ice clouds; For $T > -40^\circ\text{C}$, the
228 occurrence of clouds including mixed-phase clouds ($-40^\circ\text{C} < T \leq 0^\circ\text{C}$) and warm
229 clouds ($T > 0^\circ\text{C}$) are defined by the conditions of either $N_i > 0.1 \text{ L}^{-1}$ or $N_d > 1 \text{ cm}^{-3}$. Here,
230 we only analyze CDP measurements with $N_d > 1 \text{ cm}^{-3}$ to avoid measurement noise as
231 determined by the sensitivity of the instrument.

232 The HIPPO dataset has been previously used for statistical analyses of ice cloud

233 formation conditions and microphysical properties, such as the conditions of the
234 birthplaces of ice clouds – the ice supersaturated regions, the evolutionary trend of
235 RH and N_i inside cirrus clouds, and hemispheric differences in these cloud properties
236 (Diao et al., 2013; 2014a, b). In this study, we will use these observations to evaluate
237 CAM5 simulation of ice clouds. We use 10-second averaged measurements (~2.3 km
238 horizontal resolution) which are derived from 1 Hz (~230 m horizontal resolution)
239 observations. Although variations are found (mostly within a factor of 2 and
240 sometimes up to 2-3 for N_i , IWC and λ) within 10-second intervals, the 10-second
241 averaged observations shown in this study are similar to those based on 1-second
242 measurements.

243

244 **3 Model and experiment design**

245 **3.1 Model**

246 This study uses version 5.3 of CAM5 (Neale et al., 2012), the atmospheric
247 component of NCAR Community Earth System Model (CESM). The cloud
248 macrophysics scheme in CAM5 provides an integrated framework for treatment of
249 cloud processes and imposes full consistency between cloud fraction and cloud
250 condensates (Park et al., 2014). Deep cumulus, shallow cumulus, and stratus clouds
251 are assumed to be horizontally distributed in each grid layer without overlapping with
252 each other. Liquid stratus and ice stratus are assumed to have a maximum horizontal
253 overlap with each other. Stratiform microphysical processes are represented by a
254 two-moment cloud microphysics scheme (Morrison and Gettelman et al., 2008;

255 hereafter as version 1 of MG scheme (MG1)). MG1 was improved by Gettleman et al.
256 (2010) to allow for ice supersaturation. It is coupled with a modal aerosol model
257 (MAM, Liu et al. (2012a)) for aerosol-cloud interactions. Cloud droplets can form via
258 the activation of aerosols (Abdul-Razzak and Ghan, 2000). Ice crystals can form via
259 the homogeneous nucleation of sulfate aerosol, and/or heterogeneous nucleation of
260 dust aerosol (Liu and Penner, 2005; Liu et al., 2007). The moist turbulence scheme is
261 based on Bretherton and Park (2009). Shallow convection is parameterized following
262 Park and Bretherton (2009), and deep convection is treated following Zhang and
263 McFarlane (1995) with further modifications by Richter and Rasch (2008).

264 Compared to the default version 5.3, the CAM5.3 version we use includes a
265 version 2 of the MG scheme (MG2) as described by Gettelman and Morrison (2015)
266 and Gettelman et al. (2015). MG2 added prognostic precipitation (i.e., rain and snow)
267 as compared with the diagnostic precipitation in MG1. Note that current version of
268 MG scheme treats cloud ice and snow as different categories with their number and
269 mass predicted, respectively (Morrison and Gettelman, 2008). To be consistent with
270 the observations, here the number and mass concentrations of cloud ice and snow are
271 combined together to get the slope parameter λ following Eidhammer et al. (2014).

272 **3.2 Experimental design for model-observation comparisons**

273 Model experiments are performed using specified dynamics, that is, online
274 calculated meteorological fields (U, V, and T) are nudged towards the GEOS-5
275 analysis (the control experiment, referred to as CTL hereafter), while water vapor,
276 hydrometeors and aerosols are calculated online by the model itself (Larmarque et al.,

User 2/23/2017 4:57 PM

Deleted: the

278 | 2012). We also conduct two experiments, one with only U and V nudged (referred to
279 | as NUG_UV) and the other with U, V, T and water vapor (Q) nudged (referred to as
280 | NUG_UVTQ). These results will be discussed in section 5. The model horizontal and
281 | vertical resolutions are $1.9^\circ \times 2.5^\circ$ and 56 vertical levels, respectively. The time step
282 | is 30 min. The critical threshold diameter for autoconversion of cloud ice to snow (D_{cs})
283 | was found to be an important parameter affecting ice cloud microphysics (e.g., Zhang
284 | et al., 2013; Eidhammer et al., 2014). D_{cs} is set to 150 μm in MG2. We also conduct
285 | two sensitive experiments using a value of 75 μm (referred to as DCS75) and 300 μm
286 | (referred to as DCS300) for D_{cs} (Table 1).

287 | In the standard CAM5 model, homogeneous nucleation takes place on sulfate
288 | aerosol in the Aitken mode with diameter greater than 0.1 μm (Gettelman et al., 2010).
289 | We conduct a sensitivity experiment (referred to as SUL) by removing this size limit
290 | (i.e., using all sulfate aerosol particles in the Aitken mode for homogeneous
291 | nucleation). Recently, Shi et al. (2015) incorporated the effects of pre-existing ice
292 | crystals on ice nucleation in CAM5, simultaneously removing the lower limit of
293 | sulfate aerosol size and the upper limit of the sub-grid updraft velocity used for the ice
294 | nucleation parameterization. Here a sensitivity experiment (referred to as PRE-ICE)
295 | with the Shi et al. (2015) modifications is conducted (Table 1).

296 | We run the model from June 2008 to December 2011 (i.e., 43 months) with the
297 | first seven months as the model spin-up. For direct comparisons between model
298 | results and observations, only model output collocated with HIPPO aircraft flights are
299 | recorded. That is, we locate the model grid boxes in which the HIPPO aircraft was

User 2/23/2017 5:22 PM

Deleted: where

User 2/23/2017 5:22 PM

Deleted: are

User 2/23/2017 5:24 PM

Deleted: nudging

303 transecting through, and then output the model results of these grid boxes at the
304 closest time stamps with respect to the flight time. In total, we have 130,577 in-situ
305 observation samples at 10-second resolution (~363 hours) for HIPPO#2-5. We note
306 that because the current CAM5 model cannot explicitly resolve the spatio-temporal
307 variability of dynamic fields and cloud properties inside a model grid box, there are
308 inevitably certain caveats in its comparison with in-situ observations. For example, as
309 the model time step is 30 min and horizontal grid spacing is ~200 km, there may be
310 cases where tens to hundreds of flight samples are located within one grid box at a
311 specific time stamp. In this study, we find that there are 1 to 170 observation samples
312 within a model grid box. Therefore, we may over-sample the model results within a
313 model grid box with multiple aircraft samples. However, we note that because of the
314 specific flight plan of the HIPPO campaign, most of the HIPPO flights were designed
315 to follow a nearly constant direction when flying from one location to the next, and
316 one vertical profile was generally achieved by about every 3 latitudinal degrees. This
317 unique flight pattern combined with the comparatively long flight hours helps to
318 provide a large amount of observation samples transecting through various climate
319 model grid boxes. In total, 635 model grid boxes are used in the direct comparisons
320 with observations. Considering that the actual horizontal area fraction of a model grid
321 box that the aircraft transected through is relatively small, derivations of grid-scale
322 mean observations which can represent the realistic characteristics for the whole grid
323 box are not possible. Nevertheless, we also derive the mean of observations within a
324 model grid box and compare them with model simulations, and the comparison results

325 are similar to those shown in Section 4. Note that vertical interpolation is taken to
326 account for the altitude variation of model variables for the direct comparison with
327 aircraft observations.

328

329 **4 Results**

330 **4.1 Cloud occurrence**

331 In this section, we will first demonstrate the model performance in simulating the
332 spatial distributions of clouds with a case study. Then we will show the overall
333 features of cloud occurrence for all comparison samples. To identify the reasons for
334 the model-observation discrepancies, we will analyze the meteorology conditions (e.g.,
335 T, Q and RH) and physics processes associated with the formation of clouds. The
336 probability density function (PDF) of ice supersaturation at clear-sky and inside ice
337 clouds will be examined.

338

339 **4.1.1 Case study – a specific cloud system**

340 During HIPPO deployment #4 and research flight 05, the GV aircraft flew from
341 the Cook Islands to New Zealand over the South Pacific Ocean on June 25–26, 2011
342 (Figure 1). Low-level clouds existed along almost all the flight tracks at 700–1000
343 hPa, and most of them were warm clouds ($T > 0^{\circ}\text{C}$). Mid-level (at 400–700 hPa) and
344 high-level clouds (at 250–400 hPa) were also observed. Generally the model captures
345 well the locations of cloud systems along the flight tracks on June 25, 2011. The
346 simulated ice clouds are located above liquid clouds and extend for thousands of

347 kilometers, which corresponds with the observed mid- to high-level clouds at
348 250–600 hPa at UTC 2200–2400 on June 25, 2011. However, the model misses the
349 low-level clouds observed on late June 25 and early June 26, and simulates a smaller
350 horizontal extent for the mid-level cloud at UTC 0230 on June 26. Overall, the
351 observed clouds on June 26 (further South) were more scattered than those on June 25.

352 The model is less capable of reproducing these scattered clouds. CAM5 is able to
353 better simulate cloud systems with larger spatial extents, since these systems are
354 controlled by the nudged large-scale meteorology.

355 Figure 2 shows the time series of RH, Q and T during the flight segment shown in
356 Figure 1. The observations show large spatial variability in RH even during the
357 horizontal flights on June 26. Overall, the simulated RH is within the range of the
358 observations but the model is unable to simulate the larger variability, which occurred
359 on sub-grid spatial scales. Both observed and simulated RH values are above 100%
360 when the model captures the clouds successfully at UTC 2240-2250 and 2310-2330
361 on June 25 and at UTC 0000-0010 on June 26 (denoted by green vertical bars),
362 although the simulated maximum grid-mean RH value is around 110%, which is
363 10-30% less than observed RH values. However, the model cannot capture some of
364 the observed clouds with large RH values within the grid boxes. For example, the
365 model misses the RH associated with low-level clouds (Figure 1) at UTC 2250-2310
366 when simulated grid-mean RH values are around 90% compared to observed values
367 of around 100%. Note that since the aircraft sampled only portions of the model grid
368 boxes, the “over-production” of cloud occurrences by the model shown in Figure 2

User 2/23/2017 5:00 PM

Deleted: better

370 (blue vertical bars) may not necessarily be the case. Thus we will focus on the cases
371 when the model captures or misses the observed clouds within the model grid boxes.

372 The spatial distributions of RH play an important role in determining whether
373 modeled clouds occur at the same times and locations as those observed. Biases in
374 either Q or T may lead to discrepancies in RH (Figs. 2d and 2f). For example, at
375 around UTC 2150 on June 25, higher RH in the model is caused by the larger
376 simulated Q; at UTC 2250 on June 25, simulated lower RH is mainly caused by the
377 warmer T. To illustrate whether T or Q biases are the main cause for the RH biases,
378 we calculate the offline distribution of RH by replacing the modeled Q or T with the
379 aircraft observations, as shown in Figures 3a and 3b, respectively. After adopting the
380 observed T spatial distributions, the updated RH still misses the RH variability around
381 UTC 0230 – 0400 on June 26, while by adopting the observed Q spatial distribution,
382 the updated RH distribution is very close to the observed one. Thus, in this case study
383 the lack of a large RH spatial variability shown in the observations mainly results
384 from the model's lack of sub-grid scale variability of Q rather than that of T.

385 **4.1.2 Synthesized analyses on cloud occurrences and cloud fraction**

386 The overall performance of the model in simulating the cloud occurrences for all
387 flights in HIPPO 2–5 is shown in Table 2. In the model, clouds often occupy a
388 fraction of a grid box, and cloud fraction together with in-cloud liquid/ice number
389 concentrations are used to represent the occurrence of stratus clouds (Park et al.,
390 2014). For HIPPO, the occurrence of clouds is derived by combining the observations
391 of both liquid and ice number concentrations as described in section 2. In total, the

392 model captures 79.8% of observed cloud occurrences inside model grid boxes. For
393 different cloud types, the model reproduces the highest fraction (94.3%) of observed
394 ice clouds, and the second highest fraction (86.1%) for mixed-phase clouds. In
395 contrast, the model captures only about half (49.9%) of observed warm clouds. As
396 depicted in the case study in section 4.1.1, the missing of cloud occurrences are
397 mainly due to the insufficient representation of sub-grid variability of RH in the
398 model. Next we will further quantify the contribution of sub-grid water vapor and
399 temperature variations to sub-grid variability of RH.

400 **4.1.3 Decomposition of relative humidity biases**

401 The formation of liquid droplets/ice crystals depends on dynamical and
402 thermodynamical conditions such as temperature, water vapor and updraft velocity
403 (Abdul-Razzak and Ghan, 2000; Liu et al., 2007, 2012b; Gettelman et al., 2010). The
404 fraction of liquid/ice stratus clouds is calculated empirically from the grid-mean RH
405 (Park et al., 2014). Thus RH is an important factor for both model representations of
406 cloud occurrences and cloud fraction. RH is a function of pressure, temperature and
407 water vapor. Since we only compare observations with the simulation results on the
408 same pressure levels, differences of RH (dRH) between simulations and observations
409 (i.e., model biases in RH) only result from the differences in temperature and water
410 vapor. We calculate the contributions of biases in water vapor and temperature to the
411 biases in RH following the method that was used to analyze RH spatial variability in
412 Diao et al. (2014a). RH_o (observations) and RH_m (model results) are calculated as:

413
$$RH_m = \frac{e_m}{e_{s,m}}, RH_o = \frac{e_o}{e_{s,o}} \quad (2)$$

414 where e_o and e_m are observed and simulated water vapor partial pressure, respectively,
 415 and $e_{s,o}$ and $e_{s,m}$ are observed and simulated saturation vapor pressure over ice ($T \leq 0^\circ\text{C}$)
 416 or over water ($T > 0^\circ\text{C}$) in the observations or the model, respectively.

417 Here dRH is calculated from the difference of simulated grid-mean RH (with
 418 vertical variances taken into account by the vertical interpolation) and in-situ

419 observations. We define $de = (e_m - e_o)$, and $d\left(\frac{1}{e_s}\right) = \frac{1}{e_{s,m}} - \frac{1}{e_{s,o}}$, therefore dRH is

420
$$dRH = RH_m - RH_o = de \cdot \frac{1}{e_{s,o}} + e_o \cdot d\left(\frac{1}{e_s}\right) + de \cdot d\left(\frac{1}{e_s}\right) \quad (3)$$

421 Thus dRH can be separated into three terms: the first term is the contribution from the
 422 water vapor partial pressure (dRH_q), the second term from temperature (dRH_T), and
 423 the third term for concurrent impact of biases in temperature and water vapor
 424 ($dRH_{q,T}$).

425 Figure 4 shows the contributions of these three terms to dRH for different
 426 temperature ranges. All the three terms as well as dRH are given in percentage. The
 427 intercepts and slopes of linear regression lines for dRH_q versus dRH , dRH_T versus
 428 dRH , and $dRH_{q,T}$ versus dRH are also presented. As temperature is constrained by
 429 GEOS-5 analysis, the bias in temperature is reduced (although not eliminated) to
 430 mostly within $\pm 7^\circ\text{C}$. A considerable amount of discrepancy in RH exist between
 431 model and observations. The model successfully captures the clouds (green symbols)
 432 when the simulated RH is close to observations in all the three temperature ranges.
 433 The model tends to miss the clouds (red symbols) when lower RH is simulated, and

434 produces spurious clouds (blue symbols) when higher RH is simulated. Regarding the
435 contributions of dRH_q and dRH_T to dRH , the slopes of the linear regression for dRH_q
436 versus dRH are 0.748, 0.933 and 0.786 for $T \leq -40^\circ\text{C}$, $-40^\circ\text{C} < T \leq 0^\circ\text{C}$ and $T > 0^\circ\text{C}$,
437 respectively, which are much larger than those for dRH_T versus dRH (0.087, 0.072
438 and 0.210 for the three temperature ranges, respectively). This indicates that most of
439 the biases in RH are contributed by the biases in water vapor (dRH_q). However, for
440 $T > 0^\circ\text{C}$, although dRH_q still dominates, dRH_T contributes notably to 21% of the RH
441 biases. For $T \leq -40^\circ\text{C}$, $dRH_{q,T}$ also contributes about 17% to dRH , indicating
442 concurrent impact from biases of T and water vapor. In contrast, for $-40^\circ\text{C} < T \leq 0^\circ\text{C}$
443 and $T > 0^\circ\text{C}$, the contributions of $dRH_{q,T}$ to dRH are negligible. We note that the slopes
444 of linear regression lines for dRH_q versus dRH and dRH_T versus dRH indicate the
445 average contributions from water vapor and temperature biases to the RH biases,
446 respectively. The values of dRH_T can occasionally reach up to $\pm 100\%$, which
447 suggests the large impact from temperature biases in these cases. In addition, the
448 dRH_T and dRH_q terms can have the same (opposite) signs, which would lead to larger
449 (lower) total biases in RH. The coefficients of determination, R^2 , for the linear
450 regressions indicate that dRH_q versus dRH has a much stronger correlation than that
451 of dRH_T versus dRH .

452 **4.1.4 Ice supersaturation**

453 Ice nucleation only occurs in the regions where ice supersaturation exists.
454 Different magnitudes of ice supersaturation are required to initiate homogeneous and
455 heterogeneous nucleation (Liu and Penner, 2005). The distribution of ice

456 supersaturation may provide insights into the mechanisms for ice crystal formation
457 (e.g., Haag et al., 2003). In CAM5, ice supersaturation is allowed (Gettelman et al.,
458 2010). Homogeneous nucleation occurs when $T \leq -35^\circ\text{C}$ and ice supersaturation
459 reaches a threshold ranging from 145% to 175%. Dust aerosol can serve as INPs
460 when $\text{RH} > 120\%$. Ice supersaturation will be relaxed back to saturation via the vapor
461 deposition process (Liu et al., 2007; Gettelman et al., 2010).

462 To examine the discrepancies in ice supersaturation between model results and
463 observations, we compare the distribution of RH for conditions in clear-sky and
464 within cirrus clouds (Figure 5). The analysis is limited to the conditions of $T \leq -40^\circ\text{C}$
465 for both model simulations and observations. In CAM5, RH diagnosed in different
466 sections of the time integration procedure can be different due to the time splitting
467 algorithm. We present here both the RH before and after the microphysical processes.

468 The observations show that ice supersaturation exists in both clear-sky and
469 inside-cirrus conditions. In clear-sky environments, the PDF of RH shows a
470 continuous decrease with RH values in subsaturated conditions, followed by a
471 quasi-exponential decrease with the RH above saturation. The maximum RH_i reaches
472 up to 150%. In cirrus clouds, most of RH values range from 50% to 150% with a peak
473 in the PDF near 100%. This feature is consistent with the results of Diao et al. (2014b),
474 who used 1-second HIPPO measurements and separated the southern and the northern
475 hemispheres for comparison.

476 The PDFs of modeled RH before and after the microphysical processes are very
477 similar except the latter one has slightly lower probability of RH_i above 140% for

478 | inside-cirrus conditions. The model is capable to simulate the occurrences of ice
479 supersaturation in both clear-sky and in-cloud conditions. However, inside cirrus
480 clouds, the simulated PDF of RH peaks around 120% instead of 100% as observed.
481 Outside the cirrus clouds (clear-sky), the model simulates a much lower probability of
482 ice supersaturation with the maximum RH value around 120%. The largest ice
483 supersaturation simulated by CAM5 under clear-sky conditions is around 20%, which
484 corresponds to the ice supersaturation of 20% assumed in the model for the activation
485 of heterogeneous nucleation. This indicates the dominant mode of heterogeneous
486 nucleation in the model. However, the observations show much higher frequencies of
487 ice supersaturations larger than 20%, indicating higher RH thresholds for
488 homogeneous nucleation or heterogeneous nucleation.

489

490 **4.2 Microphysical properties of ice clouds**

491 Together with cirrus cloud fraction, the ice crystal number concentration and size
492 distribution within cirrus clouds determine the radiative forcing of cirrus clouds. In
493 this section, we will present the evaluation of modeled microphysical properties of
494 cirrus clouds for $T \leq -40^\circ\text{C}$. As measurements of ice crystal number concentration
495 include both ice and snow crystals, for comparison with observations, we combine the
496 cloud ice and snow simulated in the model (hereafter referred as ice crystals).
497 Following Eidhammer et al. (2014), the slope and intercept parameters of the gamma
498 function for the ice crystal size distribution simulated by the model are derived from
499 the total number concentration and mass mixing ratio of cloud ice and snow, which

User 2/23/2017 5:01 PM

Deleted: Compared to the observations, t

User 2/27/2017 3:32 PM

Deleted: can

502 are the integrations of the first and third moments of the size distribution function.
503 The simulated number concentration of ice crystals with sizes larger than 75 μm is
504 calculated by the integration of gamma size distributions from 75 μm to infinity. The
505 simulated IWC for ice crystals with sizes larger than 75 μm is also derived by
506 integrating the mass concentration of cloud ice and snow from 75 μm to infinity. We
507 note that about 94% of total cirrus cloud samples are at temperatures between -60°C
508 and -40°C .

509 **4.2.1 Ice crystal size distribution**

510 Direct comparison of the slope parameter (λ) for ice crystal size distributions is
511 shown in Figure 6. The slope parameter λ determines the decay rate of a gamma
512 function in relation to the increasing diameter. With a larger λ , the decay of a gamma
513 function with increasing size is faster and there are relatively fewer large ice crystals.
514 The number-weighted mean diameter can be defined as the inverse of λ (i.e., λ^{-1}). As
515 shown in Figure 6, the observed λ is generally within the range from 10^3 to 10^5 m^{-1} .
516 The model reproduces the magnitude of λ for some of the observations, but tends to
517 overestimate the observations for smaller λ values (10^3 to 10^4 m^{-1}). This indicates that
518 the model produces higher fractions of ice crystals at smaller sizes, and the
519 number-weighted mean diameter is underestimated. Moreover, the model generally
520 simulates λ in a narrower range of 7.5×10^3 to $7 \times 10^4 \text{ m}^{-1}$ for the three experiments with
521 different D_{cs} (CTL, DCS75, DCS300). SUL and PRE-ICE simulate a wider range of λ
522 which is comparable to the observations but tends to shift λ to larger values (5×10^4 to
523 $1 \times 10^5 \text{ m}^{-1}$). All the experiments rarely simulated the occurrence of small λ (below

524 $7.5 \times 10^3 \text{ m}^{-1}$).

525 Figure 7 shows the relationship of λ with temperature from observations and
526 model simulations. Here, both the geometric means and the standard deviations of λ
527 for each temperature interval of 4°C are also shown. Although the observed λ doesn't
528 monotonically decrease with increasing temperature, overall an decreasing trend can
529 be found for the whole temperature range below -40°C . This indicates a general
530 increase in the number-weighted mean diameter of ice crystals with increasing
531 temperature. The correlation between λ and temperature from HIPPO is similar to that
532 from the Atmospheric Radiation Measurements Spring Cloud Intensive Operational
533 Period in 2000 (ARM-IOP) and the Tropical Composition, Cloud and Climate
534 Coupling (TC4) campaigns as shown in Eidhammer et al. (2014), but the HIPPO
535 observations extend to lower temperatures than ARM-IOP and TC4 observations
536 where temperatures are mostly above -56°C . In addition, HIPPO observations show a
537 broader scatter range of λ , which may be because HIPPO sampled ice crystals at
538 various environment conditions as the flight tracks covered much wider areas and
539 lasted for much longer periods. The decrease of λ with increasing temperature has
540 been shown in many other studies (e.g., Heymsfield et al., 2008; 2013). Such a feature

541 is mainly due to more small ice particles at lower temperatures, which can be
542 explained by less water vapor available for ice crystal growth as well as more ice
543 crystals formed from nucleation (more likely from homogeneous nucleation than from
544 heterogeneous nucleation) at lower temperatures (Eidhammer et al., 2014).

545 Compared to the observations, the simulated mean λ is about 2-4 times larger for

User 2/27/2017 5:38 PM
Deleted: large

User 2/27/2017 5:38 PM
Deleted: higher

User 2/24/2017 10:11 AM
Deleted: and

User 2/24/2017 10:11 AM
Deleted: also

User 2/24/2017 10:10 AM
Deleted: more ice crystals formed from nucleation and

552 all the experiments, indicating that the model simulates smaller mean sizes for ice
553 crystals. The simulated λ decreases with increasing temperature, which is generally
554 consistent with the observations. In addition, the geometric standard deviations (less
555 than 2) of simulated λ are smaller than observed (around 2-3). This can be partly
556 explained by the fact that in-situ observations sampled the sub-grid variability of
557 cloud properties.

558 The difference of simulated λ is within a factor of 2 among the five experiments
559 when temperature is between -40°C and -56°C , and is larger (around 2-4) when
560 temperature is below -56°C . For the experiments with different D_{cs} , CTL and DCS75
561 simulated λ are close to each other when temperature is between -40°C and -60°C ,
562 and DCS300 simulates larger λ compared to DCS75 and CNTL. For temperatures
563 between -64°C and -72°C , CTL and DCS300 simulated λ are close to each other and
564 both are larger than that of DCS75. For the experiments with different ice nucleation
565 parameterizations, both SUL and PRE-ICE simulate larger λ than CTL especially for
566 temperatures below -56°C . SUL simulates the largest λ of all the experiments. This
567 can be explained by much larger number concentration of ice crystals (for all size
568 range, figure not shown) simulated by SUL, while IWC is not very different from
569 other experiments (section 4.2.3).

570

571 **4.2.2 Ice crystal number concentration**

572 Figure 8 shows the comparison of in-cloud number concentrations (N_i) of ice
573 crystals with diameters larger than $75\ \mu\text{m}$ between observations and simulations. The

574 magnitude of observed N_i varies by three orders of magnitude from 10^{-1} L^{-1} to 10^2 L^{-1} .
575 The model simulates reasonably well the range of N_i in cirrus clouds. However, the
576 model tends to underestimate N_i for all the experiments except DCS75. About 13%
577 (DCS75) to 30% (PRE-ICE) of observations are underestimated in the model by a
578 factor of 10. The underestimation of N_i may be partly attributed to the fact that the
579 model underestimates the ice crystal size (section 4.2.1), leading to a smaller fraction
580 of ice crystals with diameter larger than $75 \mu\text{m}$. Additional bias may result from the
581 bias in the total ice crystal number concentration, although the observations are not
582 available for comparison. We also compare simulated N_i with observed in-cloud N_i
583 averaged within the model grid boxes. We choose the flight segments with over 300
584 1-second aircraft measurements within an individual model grid and calculate the
585 average for in-cloud N_i of ice clouds ($T \leq -40 \text{ }^\circ\text{C}$). The comparison results are, however,
586 similar to those shown in Figure 8.

587 DCS75 reasonably simulates the occurrence frequency of $N_i < 1 \text{ L}^{-1}$ albeit with
588 significantly higher frequency for N_i around $1-5 \text{ L}^{-1}$ and lower frequency for N_i
589 around $5-10 \text{ L}^{-1}$. Most of the experiments cannot reproduce the occurrence frequency
590 of high N_i ($N_i > 50 \text{ L}^{-1}$) except DCS75 and PRE-ICE.

591 The relationships between N_i and temperature are shown in Figure 9. Since N_i
592 here only takes into account of ice crystals larger than $75 \mu\text{m}$, the geometric mean of
593 observed N_i generally ranges between $5-10 \text{ L}^{-1}$ for temperatures below -40°C , which
594 is 1-2 orders of magnitude lower than the number of ice crystals between $0.3-775 \mu\text{m}$
595 from observations compiled by Krämer et al. (2009) and between $10-3000 \mu\text{m}$ from

596 the SPARTICUS campaign (Zhang et al., 2013), but is comparable to the number of
597 ice crystals in the same size range from the ARM-IOP and TC4 campaigns
598 (Eidhammer et al., 2014). The geometric standard deviation of observed N_i within a
599 temperature interval of 4°C can be as high as a factor of 5.

600 The model simulates no apparent trends of N_i when temperature decreases from
601 -40°C to -60°C for the experiments CTL, DCS75 and PRE-ICE. The model simulates
602 somehow larger N_i with decreasing temperatures for the experiments DCS300 and
603 SUL. Increase of N_i at lower temperatures in SUL may indicate the occurrence of
604 homogeneous nucleation. Overall, simulated N_i is sensitive to D_{cs} . Simulated N_i is
605 also sensitive to the number of sulfate aerosol particles for homogeneous nucleation.
606 With the removal of the lower size limit (0.1 μm diameter) of sulfate aerosol particles
607 for homogeneous nucleation in the experiment SUL, simulated N_i is significantly
608 higher than that in CTL because of the substantial increase in the total ice crystal
609 number concentration in SUL, although the slope parameter in SUL is larger
610 indicating a smaller fraction of ice crystals with larger sizes (e.g., larger than 75 μm).
611 This result is consistent with that of Wang et al. (2014).

612 Although some experiments can simulate a similar magnitude of N_i as the
613 observations in some temperature ranges, most of the experiments underestimate N_i
614 and some experiments (CTL and PRE-ICE) underestimate N_i for all the temperature
615 ranges. Overall DCS75 simulates the closest magnitude of N_i with the observations
616 for temperatures from -40°C to -64°C.

617

618 4.2.3 Ice water content

619 Figure 10 shows the comparison of in-cloud IWC for ice crystals with diameter
620 larger than 75 μm between observations and simulations. The magnitude of observed
621 IWC varies by four orders of magnitude from 10^{-2} to 10^2 mg m^{-3} , which is within the
622 range of observed IWC in previous studies (Kramer et al., 2016; Luebke et al., 2016).
623 Observed IWC here is mostly larger than 1 mg m^{-3} . Compared to the observations, the
624 model for all the experiments underestimates observed IWC for 70%-95% of the
625 samples and by one order of magnitude for 25%-45% of the samples. Although the
626 model reproduces the highest occurrence frequency of IWC around $1\text{-}5 \text{ mg m}^{-3}$, the
627 model simulates more occurrence of IWC below 1 mg m^{-3} and fewer occurrence of
628 IWC above 5 mg m^{-3} .

629 The relationships between IWC and temperature are shown in Figure 11. An
630 overall increasing trend of observed IWC with temperature is found for the entire
631 temperature range. The observed relationship between IWC and temperature is
632 consistent with those shown in the previous studies (e.g., Kramer et al., 2016; Luebke
633 et al., 2016). However, the mean IWC from HIPPO is 3-5 times as large as previous
634 observations (Kramer et al., 2016; Luebke et al., 2016). Observations here only
635 account for ice crystals with diameter larger than 75 μm and thus it is less frequent
636 that observed IWC is lower than 1 mg m^{-3} . In contrast, previous studies showed that
637 IWC (including smaller sizes of ice crystals) lower than 1 mg m^{-3} was often measured
638 in observations. This contributes to the mean IWC shown here being larger than that
639 in the previous studies.

640 The simulated IWC is lower than observations for all the experiments at
641 temperatures between -40°C and -60°C where most of the observations were made.
642 The model also simulates less variation of IWC with temperature when temperature is
643 between -40°C and -60°C . When temperature is below -60°C , a steep decrease of
644 IWC is found in some experiments (e.g., CTL, SUL). Considering the large scatter of
645 IWC and relatively few samples available, this may be due to a lack of a sufficient
646 number of samples. Therefore, more observations are needed to have a robust
647 comparison for relatively low temperatures (i.e., temperatures below -60°C).
648 Simulated IWC is more sensitive to D_{cs} than to ice nucleation.

649

650 **5 Impact of Nudging**

651 In previous sections, we have nudged the simulated winds and temperature
652 towards the GEOS5 analysis, but kept the water vapor on-line calculated by the model
653 itself. We showed that the model captures a large portion (79.8%) of cloud
654 occurrences presented in the observations. We also identified the RH bias in the
655 simulation and attributed the RH bias mainly to the bias in water vapor. As the bias in
656 temperature is reduced in the nudging run compared to the free run, the attribution of
657 RH bias in the free-running model (i.e., no nudging applied) is still unclear. To
658 examine the impact of nudging strategies on the cloud occurrences and the attribution
659 of RH bias, we conducted two additional experiments: one with neither temperature
660 nor specific humidity nudged to the analysis (hereafter referred as NUG_UV), and the
661 other one with both temperature and specific humidity nudged to the analysis

662 (hereafter referred as NUG_UVTQ). Without nudging temperature, the model
663 experiment (NUG_UV) has a cold temperature bias of -1.8°C on average relative to
664 the HIPPO observations (Figure not shown). In comparison, the temperatures
665 simulated by CTL and NUG_UVTQ are more consistent with in situ aircraft
666 observations, and the mean temperature is slightly underestimated by 0.22°C and
667 0.28°C in these two experiments, respectively. By nudging specific humidity, the
668 model experiment (NUG_UVTQ) improves the simulation of grid-mean water vapor
669 concentrations by eliminating the biases especially for the cases with low water vapor
670 concentrations (less than 20 ppmv, Figure not shown). NUG_UV captures 86.0%,
671 80.9%, and 39.7% of observed ice, mixed-phase, and warm clouds, respectively,
672 which are slightly smaller than those of CTL (i.e., 94.3%, 86.1%, and 49.9%,
673 respectively). For NUG_UVTQ, although 73.5% of ice clouds are captured, the model
674 captures only 61.8% of mixed-phase clouds and 31.4% of warm clouds. The worse
675 simulation in NUG_UVTQ may be because the nudged water vapor is not internally
676 consistent with the modeled cloud physics, which deteriorates the simulation of cloud
677 occurrences. [The bias in cloud occurrences may also be related to the RH threshold](#)
678 [values used in the cloud fraction scheme in the model \(Park et al., 2014\), and further](#)
679 [study is needed to address the model sensitivity to the RH threshold values.](#)

680 As seen in Table 3, in the two new nudging experiments (NUG_UV and
681 NUG_UVTQ), modeled RH biases in the comparison with in-situ observations also
682 mainly result from the discrepancies of water vapor. The contribution of dRH_q to dRH
683 ranges from 65.8% to 92.5%, which are slightly smaller than those in CTL. In

684 NUG_UV, as the model underestimates the temperature, modeled RH is
685 systematically higher than observations, especially for $T \leq -40^\circ\text{C}$ where the absolute
686 value of RH is overestimated by 30% on average. The large T bias leads to a smaller
687 contribution from the water vapor bias (dRH_q) and a larger contribution from the
688 concurrent bias in temperature and water vapor ($dRH_{q,T}$). When both T and Q are
689 nudged in NUG_UVTQ, the contributions of the three terms to dRH are generally
690 similar to those in CTL. A larger contribution from temperature (dRH_T) is found for
691 temperature above 0°C in NUG_UVTG. This may be a result of smaller contributions
692 from either dRH_q or $dRH_{q,T}$ due to the reduced water vapor bias. We also examined
693 the in-cirrus microphysical properties simulated by these two new nudging
694 experiments. The model features such as underestimations of N_i , IWC, and mean ice
695 crystal size are similar to those in CTL and are not sensitive to the nudging strategy
696 used.

697

698 **6 Discussion and Conclusions**

699 In this study, we evaluated the macro- and microphysical properties of ice clouds
700 simulated by CAM5 using in-situ measurements from the HIPPO campaign. The
701 HIPPO campaign sampled over the Pacific region from 67°S to 87°N across several
702 seasons, making it distinctive from other previous campaigns and valuable for
703 providing insight into evaluating model performance. To eliminate the impact of
704 large-scale circulation biases on the simulated cloud processes, we ran CAM5 using
705 specified dynamics with simulated meteorology (U, V and T) nudged towards the

User 2/23/2017 5:02 PM

Deleted: which nudge the

707 GEOS-5 analysis while keeping water vapor, hydrometeors, and aerosols online
708 calculated by the model itself. Model results collocated with the flight tracks spatially
709 and temporally are directly compared with the observations. Modeled cloud
710 occurrences and in-cloud ice crystal properties are evaluated, and the reasons for the
711 biases are examined. We also examined the model sensitivity to D_{cs} and different
712 parameterizations for ice nucleation.

713 The model can reasonably capture the vertical configuration and horizontal
714 extension of specific cloud systems. In total, the model captures 79.8% of observed
715 cloud occurrences within model grid boxes. For each cloud type, the model captures
716 94.3% of observed ice clouds, 86.1% of mixed-phase and 49.9% of warm clouds. This
717 result is only modestly sensitive to whether meteorological fields (T and Q) are
718 nudged. The model cannot capture the large spatial variability of observed RH, which
719 is responsible for much of the model missing low-level warm clouds. A large portion
720 of the RH bias results from the discrepancy in water vapor, with a small portion from
721 the discrepancy in temperature. The model also underestimates the occurrence
722 frequencies of ice supersaturation higher than 20% under clear-sky conditions (i.e.,
723 outside of cirrus clouds), which may indicate too low threshold for initiating
724 heterogeneous ice nucleation in the model. In fact, a study comparing the observed
725 RH distributions with real-case simulations of the Weather Research and Forecasting
726 (WRF) model suggested that the threshold for initiating heterogeneous nucleation
727 should be set at $RHi \geq 125\%$ (D'Alessandro et al., 2017).

728 Down to the micro-scale of cirrus clouds ($T \leq -40$ °C), the model captures well the

User 2/23/2017 5:02 PM

Deleted: and

User 2/23/2017 5:03 PM

Deleted: of

Xiaohong Liu 3/9/2017 5:39 PM

Deleted: submitted

732 decreasing trend of λ with increasing temperature from $-72\text{ }^{\circ}\text{C}$ to $-40\text{ }^{\circ}\text{C}$. However, the
733 simulated λ values are about 2-4 times on average larger than observations at all the
734 $4\text{ }^{\circ}\text{C}$ temperature ranges for all the experiments with different D_{cs} and different ice
735 nucleation parameterizations. This indicates that the model simulates a smaller mean
736 size of ice crystals in each temperature range. The model is mostly able to reproduce
737 the magnitude of observed N_i (to within one order of magnitude) for ice crystals with
738 diameter larger than $75\text{ }\mu\text{m}$, yet generally underestimates N_i except for the DCS75
739 simulation. Simulated N_i is sensitive to D_{cs} and the number of sulfate aerosol particles
740 for homogeneous nucleation used in the model. No apparent correlations between the
741 mean N_i and temperature are found in the observations, while a decrease of N_i with
742 increasing temperature is found in the two simulations (DCS300 and SUL). All the
743 experiments underestimate the magnitude of IWC for ice crystals larger than $75\text{ }\mu\text{m}$.
744 The observations show an overall decreasing trend of IWC with decreasing
745 temperature while the model simulated trends are not as strong. Simulated IWC is
746 sensitive to D_{cs} but less sensitive to the different parameterizations of ice nucleation
747 examined here.

748 Current climate models have typical horizontal resolutions of tens to hundreds of
749 kilometers and are unable to represent the large spatial variability of environmental
750 conditions for cloud formation and evolution within a model grid box. A previous
751 study of Diao et al. (2014a) shows that the spatial variability of water vapor
752 dominantly contribute to the spatial variability in RH, compared with the
753 contributions from those of temperature. Here our comparisons of model simulations

754 with observations show that the biases in water vapor spatial distributions are the
755 dominant sources of the model biases in RH spatial distributions. Thus it is a priority
756 to develop parameterizations that are able to treat the sub-grid variability of water
757 vapor for climate models. There are also substantial sub-grid variations of cloud
758 microphysical properties shown in previous observational studies (e.g., Lebsock et al.,
759 2013). Currently a framework for treating the sub-grid variability of temperature,
760 moisture and vertical velocity has been developed and implemented into CAM5
761 (Bogenschutz et al., 2013). A multi-scale modeling framework has also been
762 developed to explicitly resolve the cloud dynamics and cloud microphysics down to
763 the scales of cloud-resolving models (e.g., Wang et al., 2011; Zhang et al., 2014). The
764 PDFs of sub-grid scale distributions can be sampled on sub-columns for cloud
765 microphysics (Thayer-Calder et al., 2015). With the increase of model resolutions for
766 future [global](#) model developments, the subgrid variability of temperature, moisture,
767 and cloud microphysics and dynamics will be better resolved. [In this study, we choose](#)
768 [the resolution of 1.9 degree × 2.5 degree because this resolution is still widely used in](#)
769 [climate model simulations](#). We plan to evaluate the model performances at higher
770 resolutions [and to understand the resolution dependence of model results](#).

771 Given the various environmental conditions and aerosol characteristics in the
772 atmosphere, the formation and evolution of ice crystals are not well understood, and it
773 is even more challenging for climate models to represent these processes. For the bulk
774 ice microphysics used in our model, several assumptions have to be made to simulate
775 both N_i and λ . One of them is to partition the ice crystals into cloud ice and snow

776 categories, while using D_{cs} to convert cloud ice to snow. Thus a more physical
777 treatment of ice crystal evolution such as using bin microphysics (e.g., Bardeen et al.,
778 2013; Khain et al., 2015) or a single category to represent all ice-phase hydrometeors
779 (Morrison and Milbrandt, 2015; [Eidhammer et al., 2017](#)) is needed.

780

781 **Acknowledgements**

782 X. Liu and C. Wu acknowledge support of the U.S. Department of Energy's
783 Atmospheric System Research Program (grant DE-572 SC0014239). The authors
784 would like to acknowledge the use of computational resources (ark:/85065/d7wd3xhc)
785 at the NCAR-Wyoming Supercomputing Center provided by the National Science
786 Foundation and the State of Wyoming, and supported by NCAR's Computational and
787 Information Systems Laboratory. We appreciate the efforts of the National Center for
788 Atmospheric Research (NCAR) Earth Observing Laboratory flight, technical, and
789 mechanical crews during the National Science Foundation (NSF) HIPPO Global
790 campaign, in particular the PIs of the HIPPO Global campaign: S. Wofsy, R. Keeling,
791 and B. Stephens. NCAR is sponsored by NSF. We acknowledge the support of the
792 VCSEL hygrometer by M. Diao, M. Zondlo and S. Beaton, the support of 2DC probe
793 by A. Bansemer, C. J. Webster and D. C. Rogers. We also acknowledge the funding
794 of NSFAGS-1036275 for field support and data analyses from the VCSEL
795 hygrometer in the HIPPO Global campaign. M. Diao gratefully acknowledges the
796 support from the NCAR Advanced Study Program (ASP) postdoctoral fellowship in
797 Oct 2013– Aug 2015. Final data sets and documentation from the NSF HIPPO Global

798 campaign can be accessed at <<http://hippo.ornl.gov>> in the Carbon Dioxide
799 Information Analysis Center Data Archive at Oak Ridge National Laboratory. We
800 thank T. Eidhammer from NCAR for her help on model result analysis.

801

802 **References**

- 803 Abdul-Razzak, H., and Ghan, S. J.: A parameterization of aerosol activation 2.
804 Multiple aerosol types. *J. Geophysical Research-Atmospheres* 105(D5),
805 6837-6844, 2000.
- 806 Bodas-Salcedo, A. et al.: COSP: A satellite simulation software for model assessment.
807 *Bull. Amer. Meteor. Soc.*, 92, 1023–1043, 2011.
- 808 Bardeen, C. G., A. Gettelman, E. J. Jensen, A. Heymsfield, A. J. Conley, J. Delanoë,
809 M. Deng, O. B. Toon (2013), Improved cirrus simulations in a GCM using
810 CARMA sectional microphysics, *J. Geophys. Res.*, 118,
811 doi:10.1002/2013JD020193.
- 812 Bogenschutz, P. A., Gettelman, A., Morrison, H., Larson, V. E., Craig, C., and
813 Schanen, D. P.: Higher-Order Turbulence Closure and Its Impact on Climate
814 Simulations in the Community Atmosphere Model, *J Climate*, 26, 9655-9676,
815 10.1175/JCLI-D-13-00075.1, 2013.
- 816 Boucher, O., and Coauthors: Clouds and Aerosols, in: *Climate Change 2013: The*
817 *Physical Science Basis. Contribution of Working Group I to the Fifth*
818 *Assessment Report of the Intergovernmental Panel on Climate Change*, edited by:
819 Stocker, T.F., et al., 1535, 571-657, Cambridge University Press, Cambridge,
820 United Kingdom and New York, NY, USA, 2013.
- 821 Bretherton, C. S., and Park, S.: A New Moist Turbulence Parameterization in the
822 Community Atmosphere Model, *J Climate*, 22, 3422-3448,
823 10.1175/2008JCLI2556.1, 2009.
- 824 Corti, T., Luo, B. P., Peter, T., Vömel, H., and Fu, Q.: Mean radiative energy balance
825 and vertical mass fluxes in the equatorial upper troposphere and lower
826 stratosphere, *Geophys Res Lett*, 32, L06802, 10.1029/2004GL021889, 2005.
- 827 DeMott, P. J., Cziczo, D. J., Prenni, A. J., Murphy, D. M., Kreidenweis, S. M.,
828 Thomson, D. S., Borys, R., and Rogers, D. C.: Measurements of the
829 concentration and composition of nuclei for cirrus formation, *Proceedings of the*
830 *National Academy of Sciences*, 100, 14655-14660, 10.1073/pnas.2532677100,
831 2003.
- 832 Deng, M., and Mace, G. G.: Cirrus Microphysical Properties and Air Motion Statistics
833 Using Cloud Radar Doppler Moments. Part I: Algorithm Description, *Journal of*
834 *Applied Meteorology and Climatology*, 45, 1690-1709, 10.1175/JAM2433.1,
835 2006.
- 836 Deng, M., and Mace, G. G.: Cirrus Microphysical Properties and Air Motion Statistics

- 837 Using Cloud Radar Doppler Moments. Part II: Climatology, *Journal of Applied*
 838 *Meteorology and Climatology*, 47, 3221-3235, 10.1175/2008JAMC1949.1,
 839 2008.
- 840 D'Alessandro, J., Diao, M., Wu, C., Liu, X., Chen, M., Morrison, H., Eidhammer, T.,
 841 Jensen, Jorgen B. Bansemer, A., Zondlo, M. A. and DiGangi, J. P.: Dynamical
 842 conditions of ice supersaturation in convective systems: a comparative analysis
 843 between in-situ aircraft observations and WRF simulations, *J. Geophys. Res.*
 844 *Atmos.*, 122, doi:10.1002/2016JD025994, 2017.
- 845 Diao, M., Zondlo, M. A., Heymsfield, A. J., Beaton, S. P., and Rogers, D. C.:
 846 Evolution of ice crystal regions on the microscale based on in situ observations,
 847 *Geophys Res Lett*, 40, 3473-3478, 10.1002/grl.50665, 2013.
- 848 Diao, M., Zondlo, M. A., Heymsfield, A. J., Avallone, L. M., Paige, M. E., Beaton, S.
 849 P., Campos, T., and Rogers, D. C.: Cloud-scale ice-supersaturated regions
 850 spatially correlate with high water vapor heterogeneities, *Atmos. Chem. Phys.*,
 851 14, 2639-2656, 10.5194/acp-14-2639-2014, 2014a.
- 852 Diao, M., Zondlo, M. A., Heymsfield, A. J., and Beaton, S. P.: Hemispheric
 853 comparison of cirrus cloud evolution using in situ measurements in HIAPER
 854 Pole-to-Pole Observations, *Geophys Res Lett*, 41, 4090-4099,
 855 10.1002/2014GL059873, 2014b.
- 856 Dinh, T., Fueglistaler, S., Durran, D., and Ackerman, T.: Cirrus and water vapour
 857 transport in the tropical tropopause layer – Part 2: Roles of ice nucleation and
 858 sedimentation, cloud dynamics, and moisture conditions, *Atmos. Chem. Phys.*,
 859 14, 12225-12236, 10.5194/acp-14-12225-2014, 2014.
- 860 Eidhammer, T., Morrison, H., Bansemer, A., Gettelman, A., and Heymsfield, A. J.:
 861 Comparison of ice cloud properties simulated by the Community Atmosphere
 862 Model (CAM5) with in-situ observations, *Atmos. Chem. Phys.*, 14, 10103-10118,
 863 10.5194/acp-14-10103-2014, 2014.
- 864 Eidhammer, T., Morrison, H., Mitchell, D., Gettelman, A., and Erfani, E.:
 865 Improvements in Global Climate Model Microphysics Using a Consistent
 866 Representation of Ice Particle Properties, *J. Climate*, 30, 609-629,
 867 10.1175/jcli-d-16-0050.1, 2017.
- 868 Fusina, F., Spichtinger, P., and Lohmann, U.: Impact of ice supersaturated regions and
 869 thin cirrus on radiation in the midlatitudes, *Journal of Geophysical Research:*
 870 *Atmospheres*, 112, D24S14, 10.1029/2007JD008449, 2007.
- 871 Gettelman, A., Randel, W. J., Wu, F., and Massie, S. T.: Transport of water vapor in
 872 the tropical tropopause layer, *Geophys Res Lett*, 29, 9-1-9-4,
 873 10.1029/2001GL013818, 2002.
- 874 Gettelman, A., Liu, X., Ghan, S. J., Morrison, H., Park, S., Conley, A. J., Klein, S. A.,
 875 Boyle, J., Mitchell, D. L., and Li, J. L. F.: Global simulations of ice nucleation
 876 and ice supersaturation with an improved cloud scheme in the Community
 877 Atmosphere Model, *Journal of Geophysical Research: Atmospheres*, 115,
 878 D18216, 10.1029/2009JD013797, 2010.
- 879 Gettelman, A., Liu, X., Barahona, D., Lohmann, U., and Chen, C.: Climate impacts of
 880 ice nucleation, *Journal of Geophysical Research: Atmospheres*, 117, D20201,

Xiaohong Liu 3/9/2017 5:46 PM

Deleted: submitted.

882 10.1029/2012JD017950, 2012.

883 Gettelman, A., and Morrison, H.: Advanced Two-Moment Bulk Microphysics for
884 Global Models. Part I: Off-Line Tests and Comparison with Other Schemes, *J*
885 *Climate*, 28, 1268-1287, 10.1175/JCLI-D-14-00102.1, 2015.

886 Gettelman, A., Morrison, H., Santos, S., Bogenschutz, P., and Caldwell, P. M.:
887 Advanced Two-Moment Bulk Microphysics for Global Models. Part II: Global
888 Model Solutions and Aerosol-Cloud Interactions, *J Climate*, 28, 1288-1307,
889 10.1175/JCLI-D-14-00103.1, 2015.

890 Haag, W., Kärcher, B., Ström, J., Minikin, A., Lohmann, U., Ovarlez, J., and Stohl, A.:
891 Freezing thresholds and cirrus cloud formation mechanisms inferred from in situ
892 measurements of relative humidity, *Atmos. Chem. Phys.*, 3, 1791-1806,
893 10.5194/acp-3-1791-2003, 2003.

894 Heymsfield, A. J., Field, P., and Bansemer, A.: Exponential Size Distributions for
895 Snow, *J Atmos Sci*, 65, 4017-4031, 10.1175/2008JAS2583.1, 2008.

896 Heymsfield, A. J., Schmitt, C., and Bansemer, A.: Ice cloud particle size distributions
897 and pressure-dependent terminal velocities from in situ observations at
898 temperatures from 0 to -86 C, *J. Atmos. Sci.*, 70, 4123-4154, 2013.

899 Hoose, C., and Möhler, O.: Heterogeneous ice nucleation on atmospheric aerosols: a
900 review of results from laboratory experiments, *Atmos. Chem. Phys.*, 12,
901 9817-9854, 10.5194/acp-12-9817-2012, 2012.

902 Hoyle, C. R., Luo, B. P., and Peter, T.: The Origin of High Ice Crystal Number
903 Densities in Cirrus Clouds, *J Atmos Sci*, 62, 2568-2579, 10.1175/JAS3487.1,
904 2005.

905 Jensen, E. J., Diskin, G., Lawson, R. P., Lance, S., Bui, T. P., Hlavka, D., McGill, M.,
906 Pfister, L., Toon, O. B., and Gao, R.: Ice nucleation and dehydration in the
907 Tropical Tropopause Layer, *Proceedings of the National Academy of Sciences*,
908 110, 2041-2046, 10.1073/pnas.1217104110, 2013.

909 Kärcher, B. and Spichtinger, B.: Cloud-controlling factors of cirrus, in: *Clouds in the*
910 *Perturbed Climate System: Their Relationship to Energy Balance, Atmospheric*
911 *Dynamics, and Precipitation*, edited by: Heintzenberg, J. and Charlson, R. J.,
912 *Strüngmann Forum Report*, 3536, 235-267, The MIT Press, Cambridge, MA,
913 USA, 2009.

914 Kay, J. E., Baker, M., and Hegg, D.: Microphysical and dynamical controls on cirrus
915 cloud optical depth distributions, *Journal of Geophysical Research: Atmospheres*,
916 111, D24205, 10.1029/2005JD006916, 2006.

917 Kay, J. E., et al.: Exposing global cloud biases in the Community Atmosphere Model
918 (CAM) using satellite observations and their corresponding instrument
919 simulators, *J. Clim.*, 25, 5190-5207, doi:10.1175/JCLI-D-11-00469.1, 2012.

920 Khain, A. P., Beheng, K. D., Heymsfield, A., Korolev, A., Krichak, S. O., Levin, Z.,
921 Pinsky, M., Phillips, V., Prabhakaran, T., Teller, A., van den Heever, S. C., and
922 Yano, J. I.: Representation of microphysical processes in cloud-resolving models:
923 Spectral (bin) microphysics versus bulk parameterization, *Rev Geophys*, 53,
924 247-322, 10.1002/2014RG000468, 2015.

925 Koop, T., Luo, B., Tsias, A., and Peter, T.: Water activity as the determinant for

926 homogeneous ice nucleation in aqueous solutions, *Nature*, 406, 611-614, 2000.

927 Kooperman, G. J., Pritchard, M. S., Ghan, S. J., Wang, M., Somerville, R. C. J., and
 928 Russell, L. M.: Constraining the influence of natural variability to improve
 929 estimates of global aerosol indirect effects in a nudged version of the Community
 930 Atmosphere Model 5, *J. Geophys. Res.*, 117, D23204,
 931 doi:10.1029/2012JD018588, 2012.

932 Korolev, A. V., Emery, E. F., Strapp, J. W., Cober, S. G., Isaac, G. A., Wasey, M.,
 933 and Marcotte, D.: Small Ice Particles in Tropospheric Clouds: Fact or Artifact?
 934 Airborne Icing Instrumentation Evaluation Experiment, *Bulletin of the American
 935 Meteorological Society*, 92, 967-973, 10.1175/2010BAMS3141.1, 2011.

936 Krämer, M., Schiller, C., Afchine, A., Bauer, R., Gensch, I., Mangold, A., Schlicht, S.,
 937 Spelten, N., Sitnikov, N., Borrmann, S., de Reus, M., and Spichtinger, P.: Ice
 938 supersaturations and cirrus cloud crystal numbers, *Atmos. Chem. Phys.*, 9,
 939 3505-3522, 10.5194/acp-9-3505-2009, 2009.

940 Krämer, M., Rolf, C., Luebke, A., Afchine, A., Spelten, N., Costa, A., Meyer, J.,
 941 Zöger, M., Smith, J., Herman, R. L., Buchholz, B., Ebert, V., Baumgardner, D.,
 942 Borrmann, S., Klingebiel, M., and Avallone, L.: A microphysics guide to cirrus
 943 clouds – Part 1: Cirrus types, *Atmos. Chem. Phys.*, 16, 3463-3483,
 944 doi:10.5194/acp-16-3463-2016, 2016.

945 Lamarque, J. F., Emmons, L. K., Hess, P. G., Kinnison, D. E., Tilmes, S., Vitt, F.,
 946 Heald, C. L., Holland, E. A., Lauritzen, P. H., Neu, J., Orlando, J. J., Rasch, P. J.,
 947 and Tyndall, G. K.: CAM-chem: description and evaluation of interactive
 948 atmospheric chemistry in the Community Earth System Model, *Geosci. Model
 949 Dev.*, 5, 369-411, 10.5194/gmd-5-369-2012, 2012.

950 Lawson, R. P.: Effects of ice particles shattering on the 2D-S probe, *Atmos. Meas.
 951 Tech.*, 4, 1361-1381, 10.5194/amt-4-1361-2011, 2011.

952 Lebsock, M., Morrison, H., and Gettelman, A.: Microphysical implications of
 953 cloud-precipitation covariance derived from satellite remote sensing, *Journal of
 954 Geophysical Research: Atmospheres*, 118, 6521-6533, 10.1002/jgrd.50347,
 955 2013.

956 Li, J. L. F., Waliser, D. E., Chen, W. T., Guan, B., Kubar, T., Stephens, G., Ma, H. Y.,
 957 Deng, M., Donner, L., Seman, C., and Horowitz, L.: An observationally based
 958 evaluation of cloud ice water in CMIP3 and CMIP5 GCMs and contemporary
 959 reanalyses using contemporary satellite data, *Journal of Geophysical Research:
 960 Atmospheres*, 117, D16105, 10.1029/2012JD017640, 2012.

961 Liou, K.-N.: Influence of Cirrus Clouds on Weather and Climate Processes: A Global
 962 Perspective, *Mon Weather Rev*, 114, 1167-1199,
 963 10.1175/1520-0493(1986)114<1167:IOCCOW>2.0.CO;2, 1986.

964 Liu, X., and Penner, J. E.: Ice nucleation parameterization for global models,
 965 *Meteorol Z*, 14, 499-514, 2005.

966 Liu, X., Penner, J. E., Ghan, S. J., and Wang, M.: Inclusion of Ice Microphysics in the
 967 NCAR Community Atmospheric Model Version 3 (CAM3), *J Climate*, 20,
 968 4526-4547, 10.1175/JCLI4264.1, 2007.

969 Liu, X., Easter, R. C., Ghan, S. J., Zaveri, R., Rasch, P., Shi, X., Lamarque, J. F.,

970 Gettelman, A., Morrison, H., Vitt, F., Conley, A., Park, S., Neale, R., Hannay, C.,
971 Ekman, A. M. L., Hess, P., Mahowald, N., Collins, W., Iacono, M. J., Bretherton,
972 C. S., Flanner, M. G., and Mitchell, D.: Toward a minimal representation of
973 aerosols in climate models: description and evaluation in the Community
974 Atmosphere Model CAM5, *Geosci. Model Dev.*, 5, 709-739,
975 10.5194/gmd-5-709-2012, 2012a.

976 Liu, X., Shi, X., Zhang, K., Jensen, E. J., Gettelman, A., Barahona, D., Nenes, A., and
977 Lawson, P.: Sensitivity studies of dust ice nuclei effect on cirrus clouds with the
978 Community Atmosphere Model CAM5, *Atmos. Chem. Phys.*, 12, 12061-12079,
979 10.5194/acp-12-12061-2012, 2012b.

980 Luebke, A. E., Afchine, A., Costa, A., Groß, J.-U., Meyer, J., Rolf, C., Spelten, N.,
981 Avallone, L. M., Baumgardner, D., and Krämer, M.: The origin of midlatitude
982 ice clouds and the resulting influence on their microphysical properties, *Atmos.*
983 *Chem. Phys.*, 16, 5793-5809, doi:10.5194/acp-16-5793-2016, 2016.

984 Mace, G. G., Zhang, Y., Platnick, S., King, M. D., Minnis, P., and Yang, P.:
985 Evaluation of Cirrus Cloud Properties Derived from MODIS Data Using Cloud
986 Properties Derived from Ground-Based Observations Collected at the ARM SGP
987 Site, *Journal of Applied Meteorology*, 44, 221-240, 10.1175/JAM2193.1, 2005.

988 Morrison, H., and Gettelman, A.: A New Two-Moment Bulk Stratiform Cloud
989 Microphysics Scheme in the Community Atmosphere Model, Version 3 (CAM3).
990 Part I: Description and Numerical Tests, *J Climate*, 21, 3642-3659,
991 10.1175/2008JCLI2105.1, 2008.

992 Morrison, H., and Milbrandt, J. A.: Parameterization of Cloud Microphysics Based on
993 the Prediction of Bulk Ice Particle Properties. Part I: Scheme Description and
994 Idealized Tests. *J. Atmos. Sci.*, 72, 287-311. doi:
995 <http://dx.doi.org/10.1175/JAS-D-14-0065.1>, 2015.

996 Murphy, D. M., and Koop, T.: Review of the vapour pressures of ice and supercooled
997 water for atmospheric applications, *Quarterly Journal of the Royal*
998 *Meteorological Society*, 131, 1539-1565, 10.1256/qj.04.94, 2005.

999 Neale, R. B., and Coauthors: Description of the NCAR Community Atmosphere
1000 Model (CAM 5.0), NCAR/TN-486+STR, available at:
1001 http://www.cesm.ucar.edu/models/cesm1.0/cam/docs/description/cam5_desc.pdf,
1002 2012.

1003 Park, S., and Bretherton, C. S.: The University of Washington Shallow Convection
1004 and Moist Turbulence Schemes and Their Impact on Climate Simulations with
1005 the Community Atmosphere Model, *J Climate*, 22, 3449-3469,
1006 10.1175/2008JCLI2557.1, 2009.

1007 Park, S., Bretherton, C. S., and Rasch, P. J.: Integrating Cloud Processes in the
1008 Community Atmosphere Model, Version 5, *J Climate*, 27, 6821-6856,
1009 10.1175/JCLI-D-14-00087.1, 2014.

1010 Ramanathan, V., and Collins, W.: Thermodynamic regulation of ocean warming by
1011 cirrus clouds deduced from observations of the 1987 El Nino, *Nature*, 351, 27-32,
1012 1991.

1013 Richter, J. H., and Rasch, P. J.: Effects of Convective Momentum Transport on the

1014 Atmospheric Circulation in the Community Atmosphere Model, Version 3, J
1015 Climate, 21, 1487-1499, 10.1175/2007JCLI1789.1, 2008.

1016 Shi, X., Liu, X., and Zhang, K.: Effects of pre-existing ice crystals on cirrus clouds
1017 and comparison between different ice nucleation parameterizations with the
1018 Community Atmosphere Model (CAM5), Atmos. Chem. Phys., 15, 1503-1520,
1019 10.5194/acp-15-1503-2015, 2015.

1020 Tan, X., Y. Huang, M. Diao, A. Bansemer, M. A. Zondlo, J. P. DiGangi, R. Volkamer,
1021 and Y. Hu: An assessment of the radiative effects of ice supersaturation based on
1022 in situ observations, Geophys. Res. Lett., 43, 11,039–11,047,
1023 doi:10.1002/2016GL071144, 2016.

1024 Thayer-Calder, K., Gettelman, A., Craig, C., Goldhaber, S., Bogenschutz, P. A., Chen,
1025 C. C., Morrison, H., Höft, J., Raut, E., Griffin, B. M., Weber, J. K., Larson, V. E.,
1026 Wyant, M. C., Wang, M., Guo, Z., and Ghan, S. J.: A unified parameterization of
1027 clouds and turbulence using CLUBB and subcolumns in the Community
1028 Atmosphere Model, Geosci. Model Dev., 8, 3801-3821,
1029 10.5194/gmd-8-3801-2015, 2015.

1030 Wang, M., Ghan, S., Easter, R., Ovchinnikov, M., Liu, X., Kassianov, E., Qian, Y.,
1031 Gustafson Jr, W. I., Larson, V. E., Schanen, D. P., Khairoutdinov, M., and
1032 Morrison, H.: The multi-scale aerosol-climate model PNNL-MMF: model
1033 description and evaluation, Geosci. Model Dev., 4, 137-168,
1034 10.5194/gmd-4-137-2011, 2011.

1035 Wang, M., Liu, X., Zhang, K., and Comstock, J. M.: Aerosol effects on cirrus through
1036 ice nucleation in the Community Atmosphere Model CAM5 with a statistical
1037 cirrus scheme, J. Adv. Model. Earth Syst., 06, doi:10.1002/2014MS000339,
1038 2014.

1039 Wang, M. and Penner, J. E.: Cirrus clouds in a global climate model with a statistical
1040 cirrus cloud scheme, Atmos. Chem. Phys., 10, 5449-5474,
1041 doi:10.5194/acp-10-5449-2010, 2010.

1042 Wang, P.-H., Minnis, P., McCormick, M. P., Kent, G. S., and Skeens, K. M.: A 6-year
1043 climatology of cloud occurrence frequency from Stratospheric Aerosol and Gas
1044 Experiment II observations (1985–1990), Journal of Geophysical Research:
1045 Atmospheres, 101, 29407-29429, 10.1029/96JD01780, 1996.

1046 Wang, Y., and Liu, X.: Immersion freezing by natural dust based on a soccer ball
1047 model with the Community Atmospheric Model version 5: climate effects,
1048 Environmental Research Letters, 9, 124020, 2014.

1049 Wofsy, S. C.: HIAPER Pole-to-Pole Observations (HIPPO): fine-grained, global-scale
1050 measurements of climatically important atmospheric gases and aerosols,
1051 Philosophical Transactions of the Royal Society of London A: Mathematical,
1052 Physical and Engineering Sciences, 369, 2073-2086, 10.1098/rsta.2010.0313,
1053 2011.

1054 Wylie, D. P., and Menzel, W. P.: Eight Years of High Cloud Statistics Using HIRS, J
1055 Climate, 12, 170-184, 10.1175/1520-0442-12.1.170, 1999.

1056 Zhang, C., M. Wang, H. Morrison, R. C. J. Somerville, K. Zhang, X. Liu, and J. F. Li
1057 (2014), Investigating ice nucleation in cirrus clouds with an aerosol-enabled

1058 multi-scale modeling framework, *J. Adv. Model. Earth Syst.*, 6, 998–1015,
1059 doi:10.1002/2014MS000343.

1060 Zhang, G. J., and McFarlane, N. A.: Sensitivity of climate simulations to the
1061 parameterization of cumulus convection in the Canadian Climate Centre general
1062 circulation model, *Atmosphere-Ocean*, 33, 407-446, 1995.

1063 Zhang, K., Liu, X., Wang, M., Comstock, J. M., Mitchell, D. L., Mishra, S., and Mace,
1064 G. G.: Evaluating and constraining ice cloud parameterizations in CAM5 using
1065 aircraft measurements from the SPARTICUS campaign, *Atmos. Chem. Phys.*, 13,
1066 4963-4982, 10.5194/acp-13-4963-2013, 2013.

1067 Zhang, K., Wan, H., Liu, X., Ghan, S. J., Kooperman, G. J., Ma, P. L., Rasch, P. J.,
1068 Neubauer, D., and Lohmann, U.: Technical Note: On the use of nudging for
1069 aerosol–climate model intercomparison studies, *Atmos. Chem. Phys.*, 14,
1070 8631-8645, 10.5194/acp-14-8631-2014, 2014.

1071 Zondlo, M. A., Paige, M. E., Massick, S. M., and Silver, J. A.: Vertical cavity laser
1072 hygrometer for the National Science Foundation Gulfstream-V aircraft, *Journal*
1073 *of Geophysical Research: Atmospheres*, 115, D20309, 10.1029/2010JD014445,
1074 2010.

1075

1076 Table 1. CAM5 experiments

Experiment name	Nudging	Ice microphysics parameterizations
CTL	U, V, T	Threshold diameter for autoconversion of cloud ice to snow (D_{cs}) set to 150 μm
DCS75	U, V, T	As CTL, but with $D_{cs}=75 \mu\text{m}$
DCS300	U, V, T	As CTL, but with $D_{cs}=300 \mu\text{m}$
SUL	U, V, T	As CTL, but without the lower limit (0.1 μm) for sulfate particle diameter for homogeneous freezing
PRE-ICE	U, V, T	As CTL, but with the impacts of pre-existing ice crystals on ice nucleation (Shi et al., 2015)
NUG_UV	U, V	As CTL
NUG_UVTQ	U, V, T, Q	As CTL

1077

1078

1079

1080 Table 2. The numbers of cloud occurrences in the 10-second averaged observations
1081 (N_{obs}), as well as those that CAM5 captures (N_{cap}) or misses (N_{mis}) the observed
1082 clouds within the model grid boxes for different temperature ranges. The ratio of N_{cap}
1083 and N_{mis} to N_{obs} are given in parenthesis next to them, respectively.

Cloud type	Temperature ranges	N_{obs}	N_{cap}	N_{mis}
Ice cloud	$T \leq -40^\circ\text{C}$	3101	2925 (94.3%)	176 (5.7%)
Mixed-phase cloud	$-40^\circ\text{C} < T \leq 0^\circ\text{C}$	8768	7546 (86.1%)	1222 (13.9%)
Warm cloud	$T > 0^\circ\text{C}$	3334	1665 (49.9%)	1669 (50.1%)
All		15203	12136 (79.8%)	3067 (20.2%)

1084

1085

1086 Table 3. The intercepts and slopes of the regression lines (i.e., $Y=a+b*X$) for dRH_q
 1087 versus dRH , dRH_T versus dRH , and $dRH_{q,T}$ versus dRH in the three experiments CTL,
 1088 NUG_UV, and NUG_UVTQ, respectively. The coefficients are determination (i.e., R^2)
 1089 for each regression line are also presented.

		$T \leq -40^\circ\text{C}$			$-40^\circ\text{C} < T \leq 0^\circ\text{C}$			$T > 0^\circ\text{C}$		
		<i>a</i>	<i>b</i>	R^2	<i>a</i>	<i>b</i>	R^2	<i>a</i>	<i>b</i>	R^2
CTL	dRH_q	5.209	0.748	0.663	4.632	0.933	0.786	0.177	0.786	0.840
	dRH_T	-0.798	0.087	0.071	-3.013	0.072	0.039	-0.706	0.210	0.262
	$dRH_{q,T}$	-4.411	0.165	0.241	-1.619	-0.005	.0004	0.529	0.004	0.001
NUG_UV	dRH_q	-16.85	0.723	0.562	-5.589	0.866	0.614	-5.207	0.658	0.698
	dRH_T	29.96	-0.103	0.024	10.09	-0.013	.0005	4.804	0.265	0.188
	$dRH_{q,T}$	-13.11	0.380	0.487	-4.498	0.148	0.088	0.402	0.078	0.085
NUG_UVTQ	dRH_q	-2.851	0.813	0.770	2.260	0.925	0.672	-1.773	0.733	0.761
	dRH_T	3.964	0.073	0.040	-0.265	0.094	0.038	1.892	0.308	0.311
	$dRH_{q,T}$	-1.113	0.114	0.262	-1.996	-0.019	0.003	-0.119	-0.041	0.095

1090
 1091

1092

1093 **Figure captions:**

1094 Figure 1. Cloud occurrences simulated by CAM5 (blue and green shaded areas)
1095 compared with HIPPO observations (crosses) during HIPPO#4 Research Flight 05
1096 (H4RF05) from Rarotonga, the Cook Islands (21.2°S, 159.77°W) to Christchurch,
1097 New Zealand (43.48°S, 172.54°E) on June 25–26, 2011. Modeled in-cloud ice crystal
1098 number concentration and cloud droplet number concentration are denoted by blue
1099 and green shaded areas, respectively. Three temperature ranges are used to categorize
1100 the combined measurements of 2DC and CDP probes. The criteria for defining
1101 observed cloud occurrences are described in section 2.

1102 Figure 2. Spatial variabilities of RH, water vapor (Q), and temperature (T) from
1103 CAM5 simulation and HIPPO observation (left), and their differences (right).
1104 Absolute difference between CAM5 and HIPPO is shown for RH and T, while the
1105 ratio between CAM5 and HIPPO is shown for Q. Model performances are denoted by
1106 shaded vertical bars: green (red) denotes when the model captures (misses) the
1107 observed cloud occurrences, and blue denotes when the model simulates a cloud that
1108 is not present in the observation.

1109 Figure 3. As Figure 2a, but for RH recalculated by replacing the model output with
1110 either (a) observed Q or (b) observed T values.

1111 Figure 4. Corresponding (top) dRH_q versus dRH , (middle) dRH_T versus dRH , and
1112 (bottom) $dRH_{q,T}$ versus dRH (unit: %) for different temperature ranges. The colors
1113 indicating three types of model performances in simulating clouds as described in
1114 Fig.2: green (“captured”), red (“missed”) and blue (“overproduced”). The black lines
1115 denote the linear regressions of the samples (i.e., $Y=a+b*X$), and the intercept (i.e., a)
1116 and slope (i.e., b) of the regression lines as well as the coefficient of determination
1117 (i.e., R^2) are shown in the legend.

1118 Figure 5. Observed and simulated probability density functions (PDFs) of relative
1119 humidity with respect to ice (RH_i, unit: %) for $T \leq -40^\circ\text{C}$ separated into clear-sky and
1120 in-cirrus conditions. PDFs of RH_i before and after cloud microphysics in the
1121 simulations are both shown. The RH_i is binned by 2% for the calculation of PDF. The
1122 PDFs (when RH_i>100%) follow an exponent decay: $\ln(\text{PDF})=a+b*\text{RH}_i$. The values
1123 of a and b for each PDF are also shown in dark red (observed), dark blue (simulated
1124 before ice nucleation), and dark green (simulated after cloud microphysics),
1125 respectively. Note blue lines are mostly invisible as overlaid by green lines.

1126 Figure 6. (a-e) Scatterplot of observed versus simulated slope parameter (λ) of the
1127 gamma size distribution function for each experiments, and (f) the frequency of λ for
1128 each range. Note that all the comparisons are restricted to the cases when the model
1129 captures observed ice clouds ($T \leq -40$ °C).

1130 Figure 7. λ versus temperature from the measurements and simulations. The lines are
1131 the geometric mean binned by 4°C, with the vertical bars denoting the geometric
1132 standard deviation. Note that the comparisons are restricted to the cases when the
1133 model captures the observed ice clouds ($T \leq -40$ °C).

1134 Figure 8. As Figure 6, but for the number concentrations (N_i) of ice crystals with
1135 diameters larger than 75 μm for all the experiments. Note that both the comparisons
1136 are restricted to the cases when the model captures observed ice clouds ($T \leq -40$ °C).

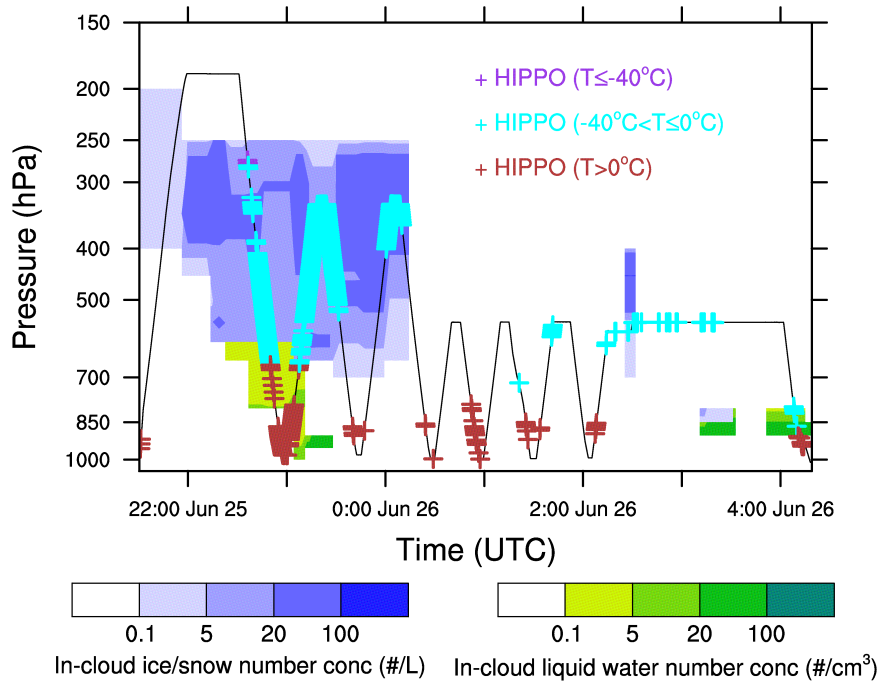
1137 Figure 9. As Figure 7, but for N_i .

1138 Figure 10. As Figure 8, but for the comparison of ice water content (IWC).

1139 Figure 11. As Figure 9, but for ice water content (IWC) versus temperature.

1140

1141



1142

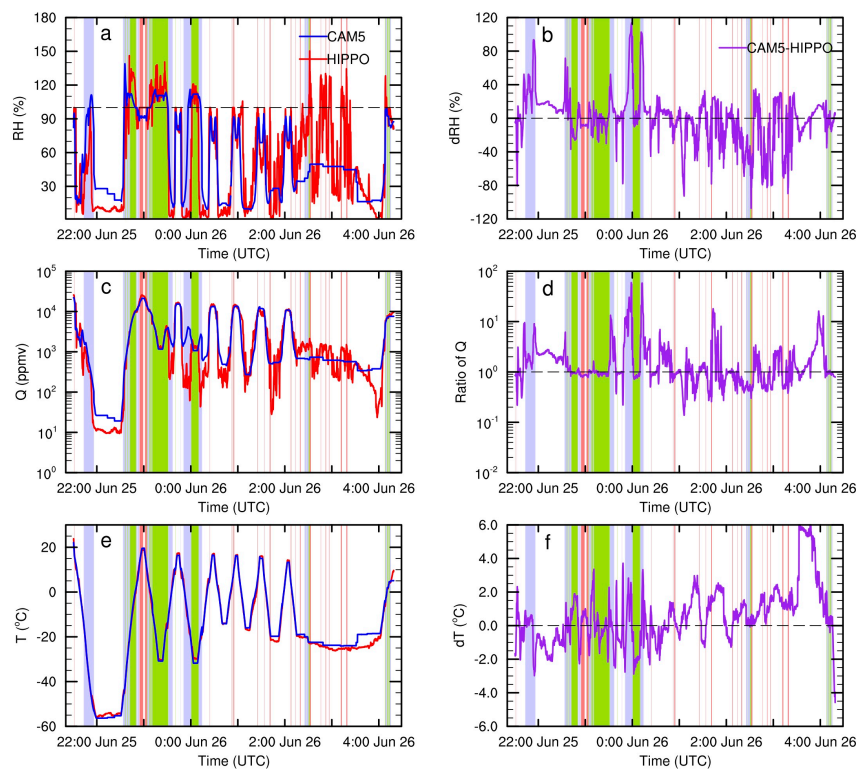
1143 Figure 1. Cloud occurrences simulated by CAM5 (blue and green shaded areas)
 1144 compared with HIPPO observations (crosses) during HIPPO#4 Research Flight 05
 1145 (H4RF05) from Rarotonga, the Cook Islands (21.2°S, 159.77°W) to Christchurch,
 1146 New Zealand (43.48°S, 172.54°E) on June 25–26, 2011. Modeled in-cloud ice crystal
 1147 number concentration and cloud droplet number concentration are denoted by blue
 1148 and green shaded areas, respectively. Three temperature ranges are used to categorize
 1149 the combined measurements of 2DC and CDP probes. The criteria for defining
 1150 observed cloud occurrences are described in section 2.

Unknown

Formatted: Font:(Default) Times New Roman, 12 pt

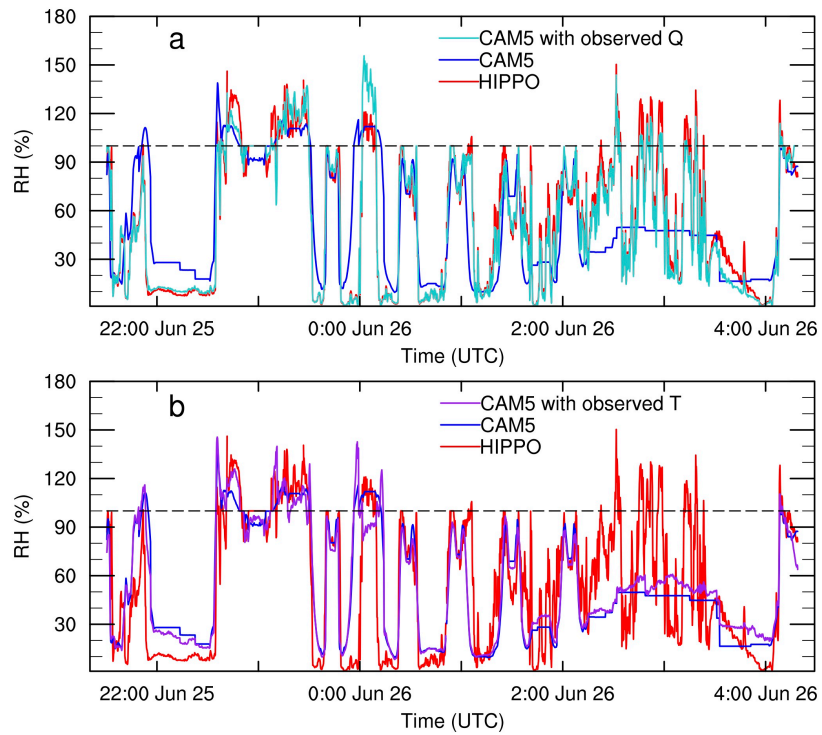
User 2/27/2017 11:17 AM

Deleted:



1152

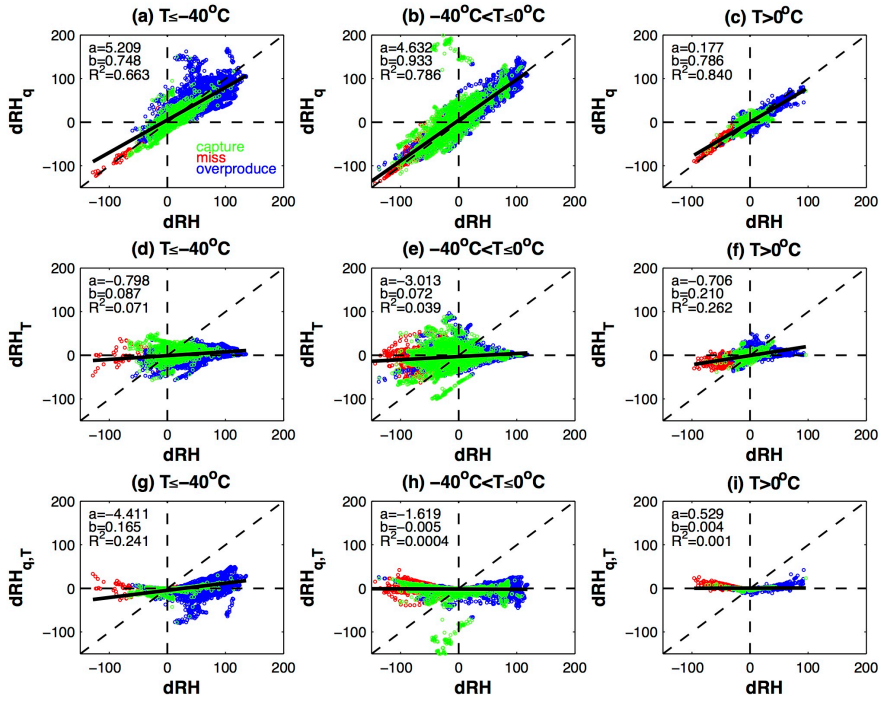
1153 Figure 2. Spatial variabilities of RH, water vapor (Q), and temperature (T) from
 1154 CAM5 simulation and HIPPO observation (left), and their differences (right).
 1155 Absolute difference between CAM5 and HIPPO is shown for RH and T, while the
 1156 ratio between CAM5 and HIPPO is shown for Q. Model performances are denoted by
 1157 shaded vertical bars: green (red) denotes when the model captures (misses) the
 1158 observed cloud occurrences, and blue denotes when the model simulates a cloud that
 1159 is not present in the observation.



1160

1161 Figure 3. As Figure 2a, but for RH recalculated by replacing the model output with
 1162 either (a) observed Q or (b) observed T values.

1163



1164

1165 Figure 4. Corresponding (top) dRH_q versus dRH , (middle) dRH_T versus dRH , and
 1166 (bottom) $dRH_{q,T}$ versus dRH (unit: %) for different temperature ranges. The colors
 1167 indicating three types of model performances in simulating clouds as described in
 1168 Fig.2: green (“captured”), red (“missed”) and blue (“overproduced”). The black lines
 1169 denote the linear regressions of the samples (i.e., $Y=a+b*X$), and the intercept (i.e., a)
 1170 and slope (i.e., b) of the regression lines as well as the coefficient of determination
 1171 (i.e., R^2) are shown in the legend.

1172

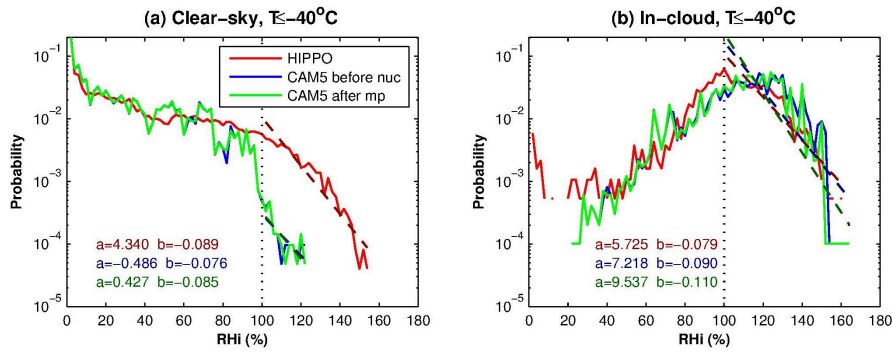
1173

1174

1175

1176

1177

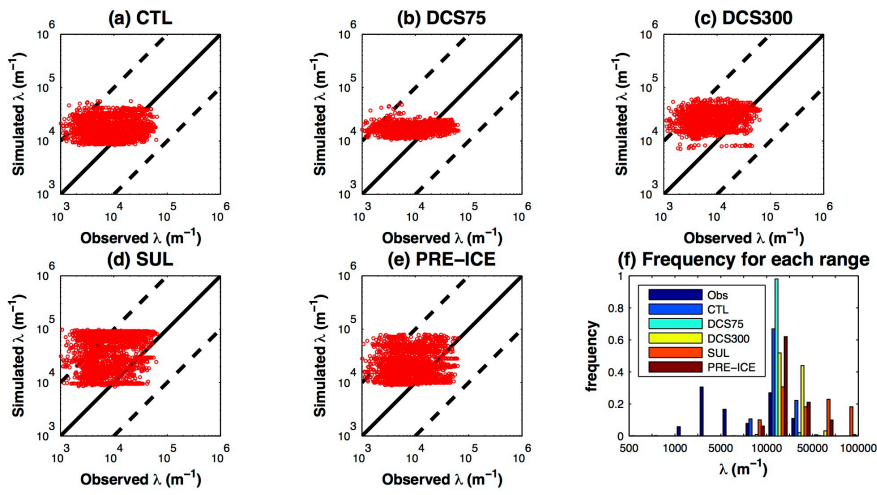


1178

1179 Figure 5. Observed and simulated probability density functions (PDFs) of relative
1180 humidity with respect to ice (RH_i , unit: %) for $T \leq -40^\circ\text{C}$ separated into clear-sky and
1181 in-cirrus conditions. PDFs of RH_i before and after cloud microphysics in the
1182 simulations are both shown. The RH_i is binned by 2% for the calculation of PDF. The
1183 PDFs (when $RH_i > 100\%$) follow an exponent decay: $\ln(\text{PDF}) = a + b \cdot RH_i$. The values
1184 of a and b for each PDF are also shown in dark red (observed), dark blue (simulated
1185 before ice nucleation), and dark green (simulated after cloud microphysics),
1186 respectively. Note blue lines are mostly invisible as overlaid by green lines.

1187

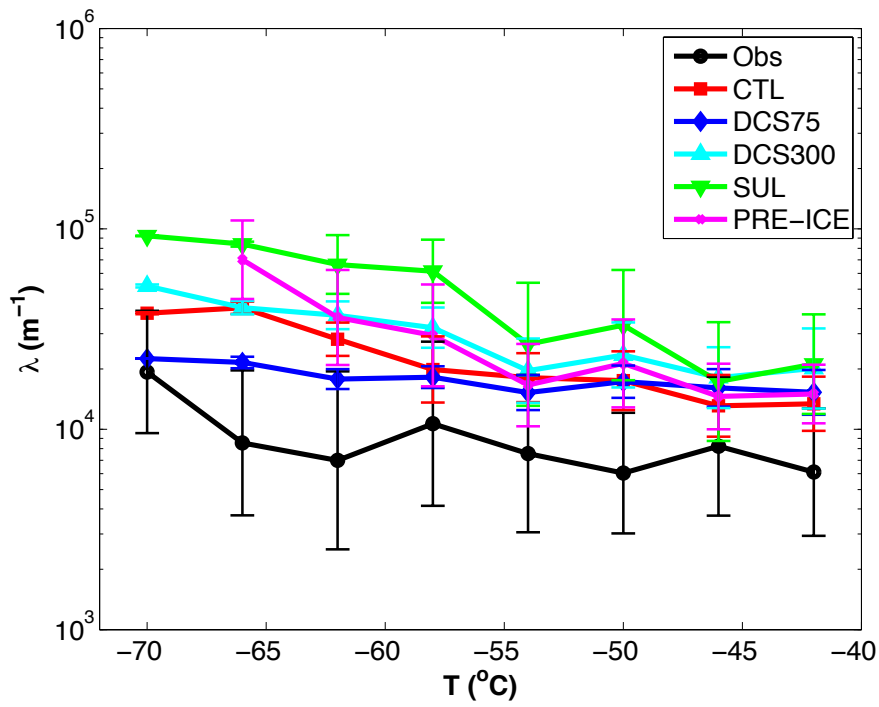
1188
1189



1190

1191 Figure 6. (a-e) Scatterplot of observed versus simulated slope parameter (λ) of the
1192 gamma size distribution function for each experiments, and (f) the frequency of λ for
1193 each range. Note that all the comparisons are restricted to the cases when the model
1194 captures observed ice clouds ($T \leq -40$ °C).

1195



1197

1198 Figure 7. λ versus temperature from the measurements and simulations. The lines are
 1199 the geometric mean binned by 4°C, with the vertical bars denoting the geometric
 1200 standard deviation. Note that the comparisons are restricted to the cases when the
 1201 model captures the observed ice clouds ($T \leq -40$ °C).

1202

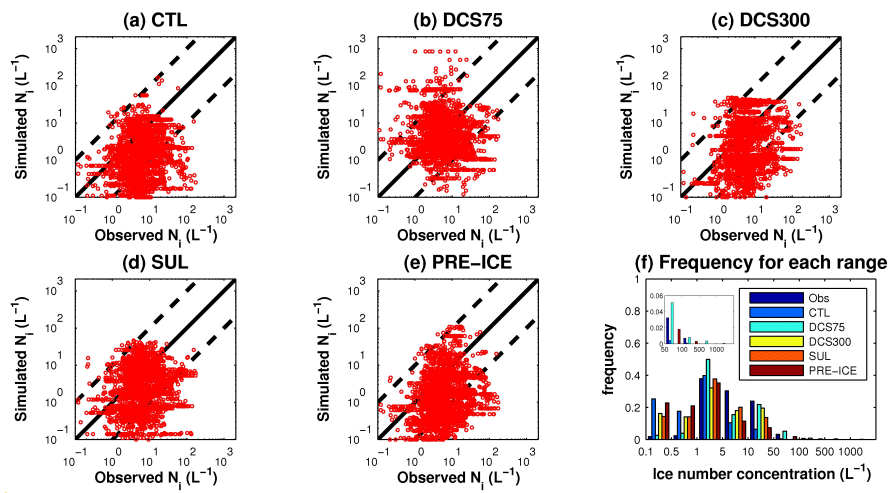
1203

1204

1205

1206

1207



1208

1209 Figure 8. As Figure 6, but for the number concentrations (N_i) of ice crystals with
 1210 diameters larger than $75 \mu\text{m}$ for all the experiments. The inset in (f) is the frequency
 1211 of N_i plotted for $N_i > 50 \text{ L}^{-1}$. Note that both the comparisons are restricted to the cases
 1212 when the model captures observed ice clouds ($T \leq -40 \text{ }^\circ\text{C}$).

1213

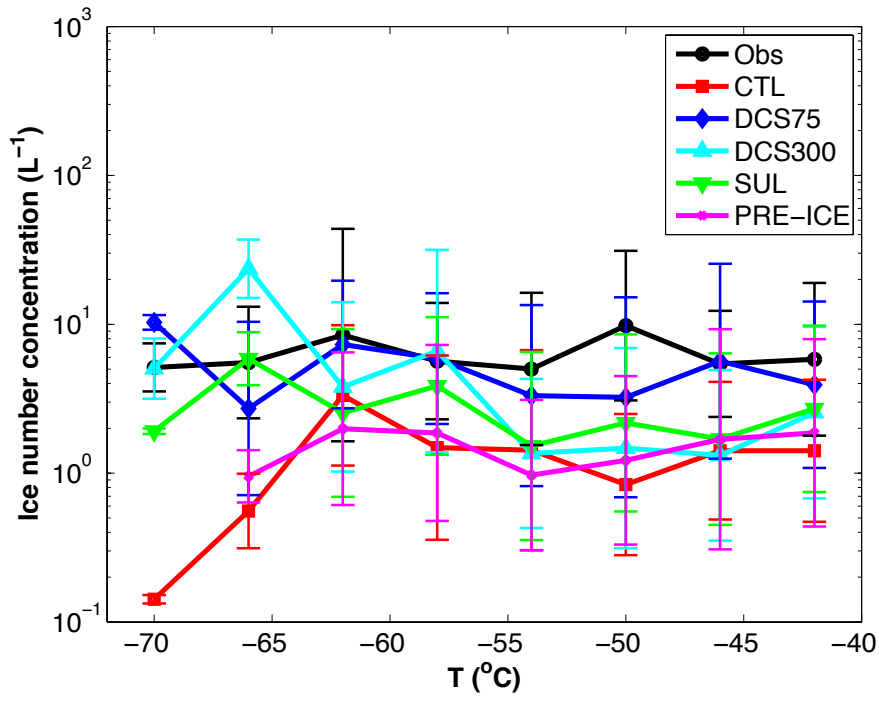
Unknown

Formatted: Font:(Default) Times New Roman, 12 pt

User 2/27/2017 11:15 AM

Deleted:

1215

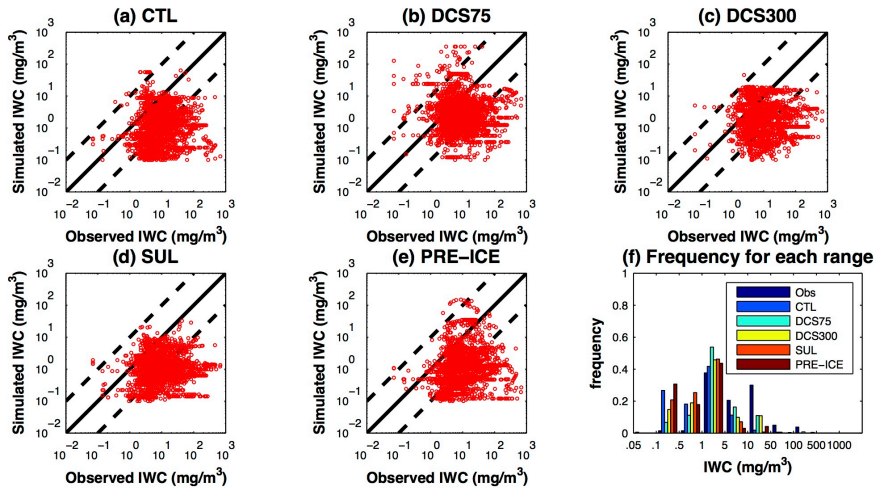


1216

1217 Figure 9. As Figure 7, but for N_i .

1218

1219

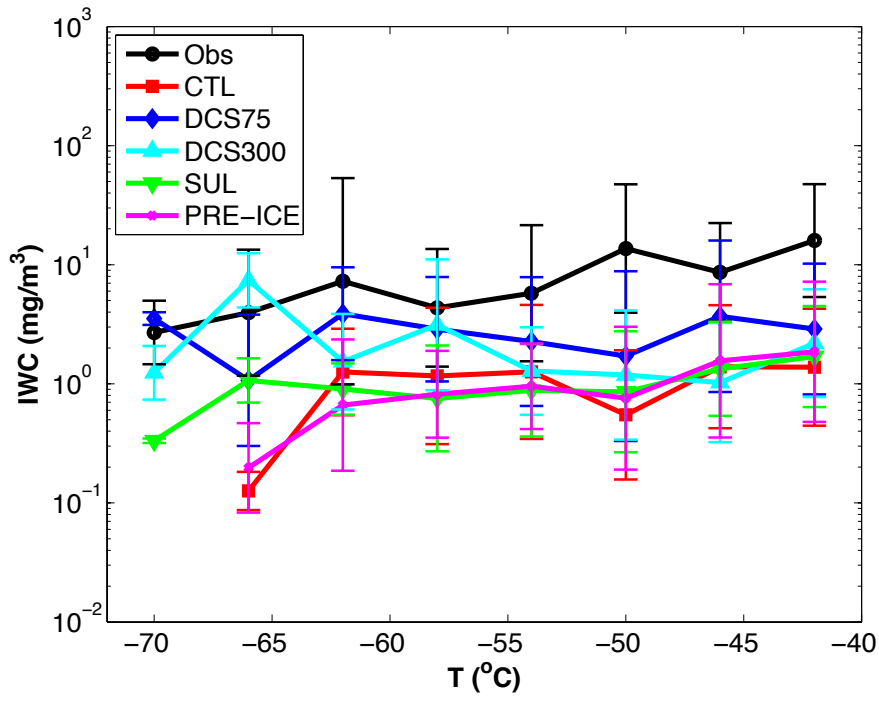


1220

1221 Figure 10. As Figure 8, but for the comparison of ice water content (IWC).

1222

1223



1224

1225 Figure 11. As Figure 9, but for ice water content (IWC) versus temperature.

1226